Soft Matter

Effect of Random Fiber Network on the Bubble Growth in Gelatin Hydrogel

Journal:	*Soft Matter*
Manuscript ID	SM-ART-04-2021-000587.R1
Article Type:	Paper
Date Submitted by the Author:	29-Aug-2021
Complete List of Authors:	Hasan, Fuad; The University of Texas at Arlington, Mechanical and Aerospace Engineering Mahmud, Khandakar; The University of Texas at Arlington, Mechanical and Aerospace Engineering Khan, Md; The University of Texas at Arlington, Mechanical and Aerospace Engineering; University of Pennsylvania, Neurosurgery Kang, Wonmo; Arizona State University, Aerospace and mechanical engineering Ashfaq, Adnan; The University of Texas at Arlington, Mechanical and Aerospace Enigneering

ARTICLE

Effect of Random Fiber Network on the Bubble Growth in Gelatin Hydrogel

Received 00th January 20xx,
Accepted 00th January 20xx

DOI: 10.1039/x0xx00000x

Fuad Hasan,[a] KAH Al Mahmud, [a] Md Ishak Khan [a], Wonmo Kang [b] and Ashfaq Adnan *[a]

In hydrodynamics, the event of dynamic bubble growth in pure liquid under tensile pressure is known as cavitation. The same event can also be observed in soft materials (e.g., elastomer, hydrogel). However, for soft materials, the bubble/cavity growth is either defined as *cavitation* if the bubble growth is elastic and reversible or as *fracture* if the cavity growth is by material failure and irreversible. In any way, the bubble growth can cause damage to soft materials (e.g., tissue) by inducing high strain and strain-rate deformation. Additionally, a high-strength pressure wave is generated upon the collapse of the bubble. Therefore, it is crucial to identify the critical condition of spontaneous bubble growth in soft materials. Experimental and theoretical observations have agreed that the onset of bubble growth in soft materials requires higher tensile pressure than pure water. The extra tensile pressure is required since the cavitating bubble needs to overcome the elastic and surface energy in soft materials. In this manuscript, we developed two models to study and quantify the extra tensile pressure for different gelatin concentrations. Both the models are then compared with the existing cavitation onset criteria of rubber-like materials. The validation is done with the experimental results of threshold tensile pressure for different gelatin concentrations. Both models can moderately predict the extra tensile pressure within the intermediate range of gelatin concentrations (3-7% [w/v]). For low concentration (~1%), the network's non-affinity plays a significant role and must be incorporated. On the other hand, for higher concentrations (~10%), the entropic deformation dominates, and strain energy formulation is not adequate.

Introduction

Cavitation is considered as one of the main driving factors that can potentially cause soft tissue damage[1–3]. The phenomenon has been studied for medical treatments[4–10], cavitation rheology[11–19], and recently, it has been linked to the Traumatic Brain Injury (TBI)[20–29]. The blast wave or impact-induced acceleration causes the intracranial pressure to drop, leading to cavitation in the brain[22–24,27–31]. A cavitating bubble can damage the surrounding materials by imposing high strain rate deformation and secondary shockwave upon collapse[3]. Therefore, it is crucial to understand the onset criteria of cavitation in soft biomaterials.

Recent studies on cavitation in soft biomaterials are based on the numerous pioneering works on hyperelastic elastomers (e.g., rubber)[32–35]. The cavitation onset criterion for a rubber block under quasistatic triaxial tension is defined as the cavity pressure (P_c) with a critical value of $5G/2$ (G is the shear modulus for small strain)[36,37]. The criterion is based on the incompressible Neo-Hookean material model and applicable to nuclei radius ranging from $0.5\ \mu m$ to $1 mm$. The radius range is only for rubber like material with higher elastic modulus and fracture toughness than typical biomaterials[38]. Gent discussed the limitation of the onset criterion in his *cautionary tale* and suggested, i) for smaller nuclei surface energy might dominate the cavity growth, ii) at large deformation, elastomers do not follow the simple kinetic theory of rubber-like elasticity, and iii) a fracture based approach based on Griffith's fracture criterion[39] might explain the higher cavity pressure for smaller nuclei[40]. The cavity pressure was estimated to be $9G$ for $0.5\ \mu m$ nuclei and even more for much smaller nuclei when fracture energy is considered[41]. More realistic material models have also been introduced with an *energy limiter* to study cavitation in rubber[42,43]. However, Lopez-Pamies argued that cavitation needs to be investigated as dynamic deformation since inertia and viscosity play a significant role in bubble dynamics and material nonlinearity[44–46]. He also pointed out that the agreement between theoretical and experimental observations is poor and suggested that the microscopic mechanism of rubber fracture needs to be incorporated for further study[47]. Indeed, all the references mentioned above did not consider the heterogeneity posed by the rubber microstructure. The argument raises the question of the application of the cavitation criterion of rubber to biomaterials. The inherent microstructure of hydrogel and rubber are quite different. The random fiber network (RFN) of rubber is modeled as *flexible fibers* having entropic deformation[48]. In contrast, soft biomaterials (e.g., gelatin hydrogel) have a network of *semi-flexible fibers* exhibiting enthalpy dominant deformation[49]. Moreover, studies

[a] Department of Mechanical and Aerospace Engineering, the University of Texas at Arlington.
[b] School for Engineering of Matter, Transport and Energy, Arizona State University.
[c] Woolf Hall, Room 315C, Arlington, TX 76019, USA. aadnan@uta.edu
† Footnotes relating to the title and/or authors should appear here.
Electronic Supplementary Information (ESI) available: [details of any supplementary information available should be included here]. See DOI: 10.1039/x0xx00000x

involved with cavitation in rubber generally consider the presence of a *vacuous cavity*[47]. Typical soft biomaterials are biphasic, having a solid phase of RFN and a liquid phase of water[50]. In soft materials, bubble nuclei are formed within the liquid phase as phase change phenomena between liquid and vapor. Therefore, the cavitating bubbles contain vapor and non-condensable gas in biomaterials[51].

Recent studies of cavitation in biologically relevant materials (e.g., polyacrylamide, agar and gelatin hydrogel) are primarily focused on material characterization using cavitation rheology or medical treatment using acoustic cavitation[52]. However, the *spontaneous* formation of bubble nuclei (homogeneous nucleation) under the dynamic loading conditions typical of TBI differs from recent cavitation studies in hydrogels. For example, experimental procedures related to cavitation rheology utilize a needle or focused laser pulse on creating the initial cavity in Needle Induced Cavitation (NIC) or Laser Induced Cavitation (LIC) techniques, respectively[53]. In NIC, air or water is injected at a quasistatic loading rate ($\sim 10^{-2} s^{-1}$) until unstable bubble growth occurs. The surrounding medium remain in atmospheric pressure condition, and critical cavity pressure is measured as the bubble fluid pressure ($P_c = 2S/R_0 + 5G/2$, where S is the surface tension and R_0 is the initial void size)[13,54]. Typical diameter of the needles (200-250 μm) is at least two order of magnitude larger than the length scale of the microstructure (e.g., fiber length $\sim 1\ \mu m$) of relevant materials. Therefore, the effect of the microstructure is not inherently included in NIC studies. Instead bubble growth is modeled as either elastic deformation or fracture mechanism in homogeneous continuum medium. On the other hand, LIC uses high-intensity optical field to ionize molecules and create a plasma filled cavity with high pressure and temperature[12]. The subsequent cavitation occurs at high loading rate ($100\ to\ 3{,}000\ m/s$). High-speed camera is used to capture the bubble wall motion. A modified Rayleigh-Plesset equation with added linear/nonlinear elasticity term is then incorporated with the time evolution of the bubble wall and material characterization is done (e.g., elastic modulus and viscosity). In summary, cavitation rheology focuses on material characterization by either controlling the cavity pressure or tracking the bubble wall motion. In both cases, the cavity formation is *forced* and do not address material heterogeneity.

In line with that, Acoustic Induced Cavitation (AIC) has applications in drug delivery, therapeutic treatment, diagnosis and lithotripsy[55–57]. AIC uses high frequency mechanical vibration with large pressure pulse to cavitate bubble in biomaterials. The significant difference of the loading condition typical of TBI is that the bubble growth and collapse experience one period of tension unlike high frequency driven bubble dynamics in AIC[58]. Recently, a novel drop-tower system is used to study the impact induced cavitation in gelatin[59]. The gel concentrations were varied from 1% to 7.5% [w/v] to have mechanical properties relevant to soft tissues. The loading condition (e.g., acceleration) was typical of TBI. It was observed that the threshold tensile pressure (P_T) required to cause cavitation in pure water and 1% [w/v] gel is $119\ kPa$ and $189\ kPa$, respectively. Apart from that, threshold tensile pressure increased as a function of gel concentrations. Evidently, soft biomaterials tend to withstand more tensile load before the inception of cavitation. The increased tensile load is thought to be the effects of increased surface tension, elasticity and presence of non-spherical bubble nuclei within the gel RFN[59]. In our previous study, we explored the nano bubble and gelatin RFN interaction using the molecular dynamic (MD) simulations[60]. The bubble dynamics of a pre-existing $5\ nm$ vacuous cavity in water surrounded by gelatin RFN is simulated under tri-axial tension. The threshold tensile pressure is compared with system containing pure water molecule and no gelatin RFN. The MD simulations revealed that the additional pressure is contributed by the water-gel interfacial tension, surface tension of the solution and the bending stiffness of gelatin fibers. However, nano bubbles require tensile pressure in the order of Megapascal to grow. In the TBI related cavitation study the observed critical pressure is in the range of kilopascal[22–24]. Clearly, large bubble nuclei ($\sim 1 \mu m$) are present in the real case scenario which cannot be captured by MD simulations. These studies mentioned above have led us to systematically study the threshold tensile pressure of cavitation in soft materials. Here, by *soft materials* we refer to a material system that constitutes 90% or more water and up to 10% [w/v] elastic fiber networks. While our study is applicable to any soft biomaterials, we have considered gelatin gel as the model material in this study.

In this manuscript, we have postulated that the threshold tensile pressure (P_T) is associated with two consecutive works done by the bubble: i) a portion of the tensile energy is spent on activating the bubble nuclei (nucleation pressure, P_{nuc}), and ii) the rest of the energy is spent on overcoming the surface and elastic energy (extra tensile pressure, ΔP_T). At first, we have studied the microstructure of the gel system using Scanning Electron Microscopy (SEM). Although the mean pore size is a function of the gel concentrations, the observations showed a large pore size distribution for each gel concentration. These water-filled pores are considered as the possible bubble nuclei sites. Since the initial bubble radius dominates the nucleation pressure, the pore size needs to be estimated. From the drop-tower experiments, we have observed that pure water cavitates at $120\ kPa$, which corresponds to the initial bubble radius of $1.2\ \mu m$[59]. Since there is no elastic contribution in pure water, the threshold tensile pressure is solely nucleation pressure. For low gel concentration, there exist enough large pores to accommodate bubble nuclei in the order of $\sim 1.2\ \mu m$. However, mean pore size decreases monotonically with increasing gel concentration. Therefore, both mean pore size and surface tension variation from gelatin solution to gelatin-gel are considered to give a comprehensive understanding of nucleation pressure in different gel concentrations.

Then, we have developed a novel bubble-RFN interaction model to estimate the extra tensile pressure. The model is named the *network failure model*. This approach allowed us to study the effects of microstructure on bubble growth. As mentioned earlier, the bubble needs to overcome the elastic energy imparted by the gel network. The elastic contribution comes from the strain energy stored in the network due to the bubble

growth. Our proposed model correlates bubble growth to network strain energy by considering fiber stretching, bending, and crosslink torsional energy. At quasistatic loading conditions, the gel network is said to fail via crosslink detachment. However, at the moderately high loading, the gel network fails via fiber scission at the fiber's ultimate failure strain[61]. Since the bubble grows unboundedly after certain growth, the critical condition is identified as the nearest fiber scission indicating microscopic fracture in the *network failure model*. The geometric (e.g., fiber length and diameter) and mechanical properties (e.g., fiber's elastic modulus, crosslink torsional constant) of the gel network are required to quantify the network strain energy until fibers rupture. Since swollen hydrogels have fibers that are a couple of orders larger in length than the fibers of rubber, we have developed a theoretical model of fiber length based on the work of Marmorat[62]. The SEM images of the microstructure are then used to validate the fiber length. However, it isn't easy to quantify the mechanical properties of the gel network. The gelatin network structure itself is very complex[63–65], and the topology depends on many factors, e.g., source of gelatin (bovine, porcine, etc.), manufacturing process, and sample preparation[50,66–69]. There are three approaches to studying the mechanics of the RFN[70,71]: Single fiber mechanics[72,73], unit cell model[74–77], and 3-dimensional (3D) random network model[78–88]. However, modeling 3D network requires substantial computational effort; therefore, we have adopted the *unit cell modeling* approach. We have seen successful implementation of the unit cell modeling approach in rubber elasticity with *flexible fibers*. A 3-chain[89,90], 4-chain[91,92], and 8-chain[93,94] models are the most frequently adopted unit cell models. Recently the 8-chain model of Arruda and Boyce (1993) has been modified for *semi-flexible fibers* and used to describe mechanics of fibrin network and mussel byssal threads[95,96]. Cryogenic-temperature scanning electron microscopy (cryo-SEM) observation shows that gelatin fibers form a d-periodic hierarchical structure similar to collagen fibril and connected via triple-helical gelatin strand at the crosslink[62]. Due to the collagen and gelatin network similarity, we have used the unit cell proposed by Susilo et al. (2010), who studied the micromechanics of collagen-based extra-cellular matrix (ECM)[77]. From the experimental stress-strain data of different gel concentrations, we have extrapolated the mechanical properties of the gelatin networks using the unit cell model. The same unit cell is used to develop the bubble-RFN interaction model.

In the recent trend, the bubble or cavity growth is modeled as either *cavitation* or *fracture,* respectively[53]. The event is identified as cavitation if the deformation is elastic and reversible[33,35,97,98]. On the other hand, it is defined as fracture if the growth is via material failure and is irreversible[13,38,47,54,99,100]. The transition from cavitation to fracture depends on the initial void size and the polymer volume fraction[54]. Incorporating both elastic and fracture energy into the bubble growth model revealed that the growth is simultaneously driven by cavitation and fracture[101]. As both mechanisms can be achieved at similar critical cavity pressure, it is evident that the fracture criterion is often reached during the cavitation. Therefore, finally, we have developed a continuum scale *fracture-based model* for more realistic non-linear material (e.g., Ogden material model[102]). The critical energy release rate (G_c) is used as a fracture criterion considering gel as a homogeneous medium in the macroscale. Both *fracture-based* and *network failure* models are then compared with the experimental observations of the drop-tower tests.

The present manuscript is organized as follows. First, we have defined the nucleation pressure and the extra tensile pressure. Then, we have studied the microstructure of the gelatin gels. The geometric properties of the network are evaluated from the SEM observations. The mechanical properties of the network are extracted using the unit cell model and gel stress-strain data. In the following two sections, the *network failure model* and *fracture-based model* are developed, respectively. The formulation for the extra tensile pressure from these two models is presented. In the result section, we have compared the models and discussed their validity. All findings and limitations are summarized in the conclusion section.

Cavitation Threshold Tensile Pressure (P_T)

The homogeneous nucleation theory states that atoms' random thermal motion spontaneously creates energetic particles. These particles leave the liquid phase and vaporize, thus form nucleation sites[58]. Church (2002) showed that the required energy for the nucleation increases with no bound at atmospheric pressure condition (P_{atm}) and nuclei immediately collapse[103]. A liquid subjected to negative (tensile) pressure, however, becomes *metastable*, meaning the required energy is finite for spontaneous nucleation to occur, and it depends on the strength of the tensile pressure, surface tension, and temperature.

As described by Herbertz (1988), the nucleation energy (W_{nuc}) required to form a nucleus under tension consists of three work terms[104]: i) W_c, the work to create the cavity under far-field tensile pressure (P_∞), ii) W_i, the work needed to establish the interface having surface tension (S), and iii) W_v, the energy attained by the formation of the vapor phase at vapor pressure (P_v) (see Fig. 1a),

$$\begin{aligned} W_{nuc} &= W_c + W_i - W_v \\ &= 4\pi r^2 S + \frac{4}{3}\pi r^3 (P_\infty - P_v) \end{aligned} \quad (1)$$

Eq. (1) implies that for a given tensile pressure ($P_\infty = P_{nuc}$) there exists maximum nucleation energy, $W_{nuc,max}$ $(at\ dW_{nuc}/dr = 0)$, which is required to form the bubble of the critical radius, $r = R_0$. Fig. 2 shows the energy necessary for different far-field pressure. For any positive (compressive) pressure, the required energy is unbounded. However, for negative pressure, if the available energy is less than that of maximum energy ($W_{nuc,max}$), then the bubble will have a smaller radius than the critical radius (R_0) and will eventually collapse following the left-hand side of the curve. On the other hand, the bubble will grow and cavitate if the radius is bigger than the critical value. For a simple homogenous liquid,

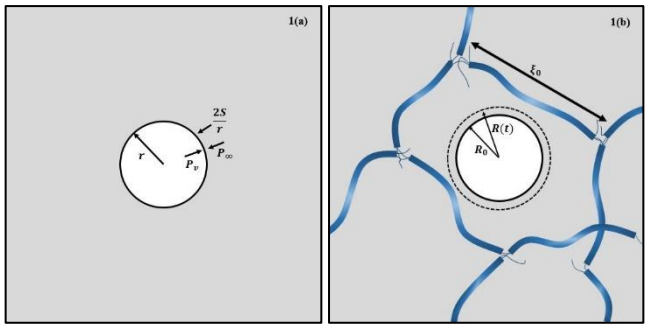

Fig. 1 Bubble nucleus in pure liquid (a) and in a gel (b). In pure liquid, the bubble pressure is in mechanical equilibrium with far-field pressure and surface tension (a). When a bubble starts to grow in the fiber network (in gel), it needs to overcome the resistance, requiring extra energy to cavitate (b).

the tensile pressure will suffice to cavitate, given that the condition is met as described above. The tensile strength of the liquid is defined as $\Delta P = (P_v - P_{nuc})$. From Eq. (1), the critical energy of nucleation can be found from the tensile strength of the liquid considering the critical tensile pressure ($P_\infty = P_{nuc}$) and saturation pressure of the bubble content,

$$W_{nuc,max} = W_{cric} = 4\pi {R_o}^2 S + \frac{4}{3}\pi {R_o}^3 \Delta P \qquad (2)$$

Now in the presence of the RFN, the required tensile pressure will be significantly higher than that of pure liquid, considering the same bubble nucleus to grow from the critical radius (R_0) (see Fig. 3). Therefore, the threshold tensile pressure for hydrogel is defined as,

$$P_T = P_{nuc} + \Delta P_T \qquad (3)$$

In the above equation, extra tensile pressure (ΔP_T) arises due to the bubble growth in the random fiber network and surface energy [59].

To the best of our knowledge, until now, only Kang et al. (2018) reported the cavitation threshold tensile pressure (P_T) for different concentrations ($C\%$ $[w/v]$) of gelatin gel and reported here in Fig. 4 from ref [59]. In their work, *Knox gelatin* is solved with water in weight to volume [w/v] ratio to prepare 1%, 2.5%, 5%, and 7.5% gelatin gels. In Fig. 4, the green dotted line indicates a 58.8% increase in threshold tension from water to 1% gelatin. The Blue dotted line is fitted with a nonlinear least

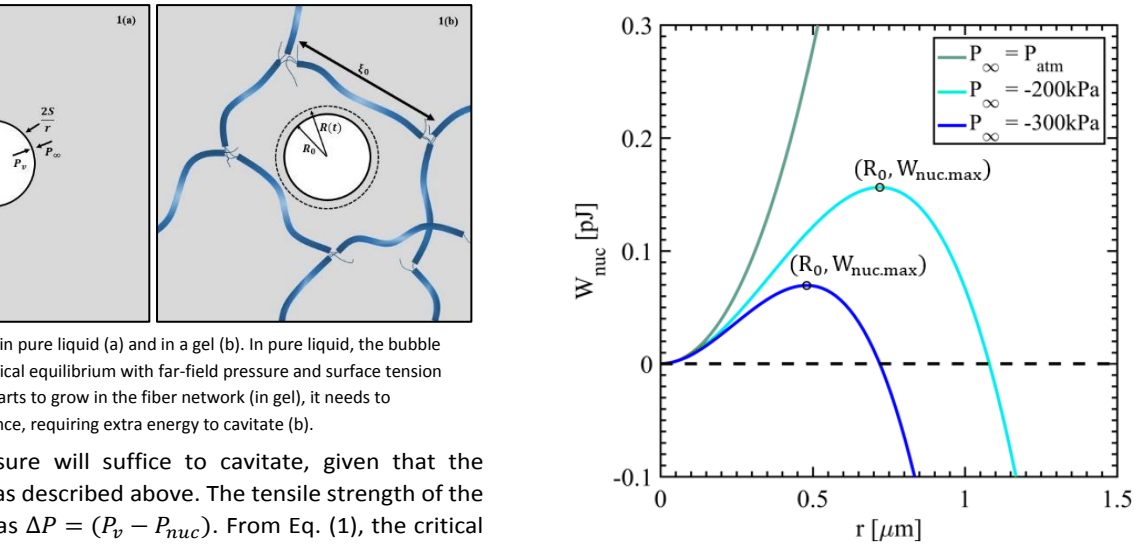

Fig. 2 Nucleation energy as a function of nuclei radius for a given pressure (Eq. (1)). The critical energy, critical radius, and nucleation pressure are indicated at each curve's peak (Eq. (2)).

square method ($R^2 = 0.93$) to show the increasing trend with gelatin concentration. From Eq. (3), it is apparent that we need to identify the contribution of P_{nuc} and ΔP_T, respectively.

Nucleation Pressure

Carey (1992) considered a system where a bubble of a radius R_0 is in a bulk liquid under tension (P_{nuc}) [105]. His formulation satisfies both mechanical and thermodynamic equilibrium for that system to be stable. At the thermodynamic equilibrium, both the vapor and the liquid phase will have the same chemical potential (μ_i),

$$\mu_l = \mu_v \qquad (4)$$

Where subscripts l and v are for the liquid and vapor phase, respectively. Now, we can use the Gibbs-Duhem relation ($d\mu_i = -sdT + vdP$) for both vapor and liquid phase, where μ_i is the chemical potential of the i^{th} phase, s is specific entropy, T is temperature, v_i is the specific volume of the i^{th} phase, and P is pressure. Integrating the Gibbs-Duhem relation from saturation condition to any arbitrary pressure at a constant temperature (T_∞),

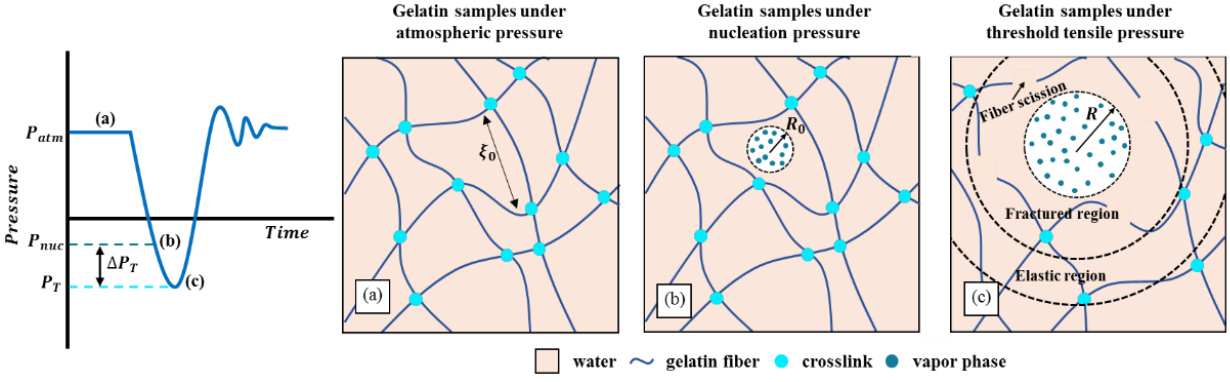

Fig. 3 A typical pressure profile for the gelatin sample is shown for the drop tower experiment of Kang et al. (2018). (a) Starting from the atmospheric condition, the corresponding RFN-bubble interaction is depicted as (b) pressure drops to nucleation pressure (P_{nuc}) and a bubble nucleaus of radius R_0forms in the water phase; (c) followed by the further pressure drops to the threshold tensile pressure (P_T) when unstable bubble growth is initiated via network failure.

$$\mu_i - \mu_{i_{sat}} = \int_{P_{sat}(T_\infty)}^{P} v_i dP \quad (5)$$

Considering bubble content as an ideal gas ($v_v = R_v T_\infty / P$), where R_v is a specific gas constant for vapor, the chemical potential for the vapor phase from the saturation condition to bubble vapor pressure (P_v) using Eq. (5) is,

$$\mu_v = \mu_{v_{sat}} + R_v T_\infty ln \left[\frac{P_v}{P_{sat}(T_\infty)}\right] \quad (6)$$

Similarly, for the incompressible liquid phase ($v_l = constant$) the chemical potential from the saturation condition to arbitrary tensile pressure (P_{nuc}) using Eq. (5) is,

$$\mu_l = \mu_{l_{sat}} + v_l \left[P_{nuc} - P_{sat}(T_\infty)\right] \quad (7)$$

Now substituting Eq. (6) and Eq. (7) into Eq. (4) and considering thermodynamic equilibrium at the saturation condition as well ($\mu_{l_{sat}} = \mu_{v_{sat}}$) we get,

$$P_v = P_{sat}(T_\infty) exp \left\{\frac{v_l[P_{nuc} - P_{sat}(T_\infty)]}{R_v T_\infty}\right\} \quad (8)$$

The above equation is based on the thermodynamic equilibrium. Considering bubble only contains saturated vapor and no noncondensable gas, then mechanical equilibrium at the formation of a bubble in the pure liquid requires,

$$P_v = P_{nuc} + \frac{2S}{R_o} \quad (9)$$

We can combine both thermodynamic equilibrium (Eq. (8)) and mechanical equilibrium (Eq. (9)) to get the desired correlation. Substituting Eq. (9) into Eq. (8), and after reorganizing we get,

$$R_0 = \frac{2S}{P_{sat}(T_\infty)\, exp\{v_l[P_{nuc} - P_{sat}(T_\infty)]/R_v T_\infty\} - P_{nuc}} \quad (10)$$

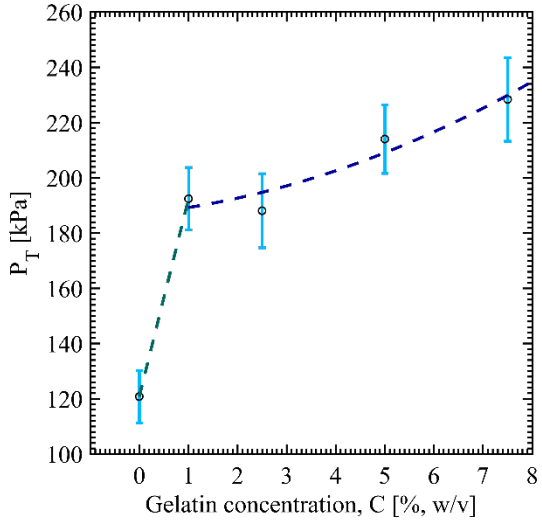

Fig. 4 Experimental observation of the threshold tensile pressure for different concentrations of gelatin gel [59]. C=0 corresponds to pure water. The vertical error bar indicates the standard deviation.

Fig. 5 plots Eq. (10) for the different surface tension of gelatin concentration. Data from the water-vapor saturation table is used for the other parameters at temperature, $T_\infty = 20^o C$. Kang et al. (2018) reported that the mean tensile pressure for water was $120 kPa$, which corresponds to a critical radius of $1.2\ \mu m$ (Fig. 5). Even for the same critical radius to cavitate in the gel system without considering the elastic contribution, the tensile nucleation pressure would be higher due to increasing surface energy (W_i) to overcome (horizontal dashed line in Fig. 5). However, the pore size within the RFN of the gel system varies with the concentration of gel, and the effect of the microstructure on the critical nuclei radius will be discussed in subsequent sections.

Extra Tensile Pressure

Considering the bubble only contains saturated vapor and no noncondensable gas, the mechanical equilibrium at forming a bubble in a pure liquid is given in Eq. (9). Where we assumed that R_o is the *reference configuration* with the stress-free surrounding medium, hence there is no elastic contribution in Eq. (9). However, when a bubble starts to grow, strain energy is stored in the network. At the *current configuration,* the pseudo-mechanical equilibrium is established at the onset of cavitation in a gel as pressure further drops from P_{nuc} to P_T (see Fig. 3),

$$P_v \left(\frac{R_o}{R}\right)^{3k} = \Delta P_T + \frac{2S}{R} + P_{RFN} \quad (11)$$

Where, P_{RFN} is the pressure contribution from the strain energy density stored in the network until the bubble stretch ratio ($\lambda_B = R/R_o$) reaches a critical value. In the above equation, we have considered vapor as an ideal gas with isothermal polytropic expansion (k=1). Therefore, the left-hand side represents the bubble pressure change as it grows. In terms of the bubble stretch ratio, Eq. (11) can be written for the extra tensile pressure as,

$$\Delta P_T = P_v \left(\frac{1}{\lambda_B}\right)^3 - \frac{2S}{R_o \lambda_B} - P_{RFN} \quad (12)$$

In summary, Eq. (3) defines the threshold tensile pressure, Eq. (10) correlates critical void size and nucleation pressure, and Eq

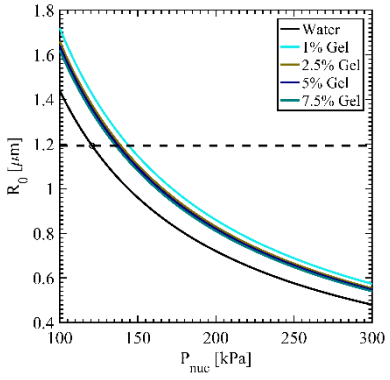

	Surface Tension, S [mN/m]
Water	72
1% Gel	86
2.5% Gel	83
5% Gel	82
7.5% Gel	81

Fig. 5 Critical bubble radius as a function of the nucleation pressure from Eq. (10). The surface tension value is taken from Ref. [59] for the gelatin gel.

(12) gives extra tensile pressure in terms of network contribution and surface energy.

Experimental Observations of Hydrogel Microstructure

Gelatin Gels Preparation

Samples are prepared with ASTM grade II standard deionized water followed by the procedure given in ref.[59]. We have prepared 3 %, 5%, and 7% [w/v] edible grade (Knox Original Gelatin, unflavoured, Kraft Foods, Northfield, IL) gelatin samples. The gelatin solution is mixed at 60^oC, 100 rpm for 30 min on a stir plate. This heated mixing step is essential for obtaining a homogeneously mixed solution and erasing thermal memory in the gelatin. Next, 4ml of the pre-mixed solution is pipetted into individual cuvettes and cured at 4^oC for 3 hours. After that, we have cut cuvettes to take out the cured sample and immediately drop the sample in a liquid nitrogen bath at -210^oC to freeze the water content. Just after freezing, the samples were transferred to a drying chamber where temperature and pressure were maintained at water sublimation temperature (-60^oC) and pressure (8 mTorr) for 24 hours for complete removal of liquid water. The freeze-dried sample is preserved in an airtight bottle to perform the SEM analysis for imaging (see Fig. S1 to Fig. S3). We have coated the samples with silver in the Compact Research Coater (CRC) 100 sputtering system before SEM/FIB analysis. Sectional SEM/FIB high-resolution image at 0.2-micron thickness was conducted in FEI Strata 400 Dual Beam FIB imaging setup (see Fig. S4). We have used 5KV power for imaging at 20000 magnification.

Mesh and Pore Size

Marmorat et al. (2016) used the cryo-SEM imaging technique to observe the gelatin supramolecular structure[62]. They showed that gelatin fibers are connected via the triple-helical gelatin strand at the crosslink. However, in low crosslink density, the distance between the crosslinks is large to allow the strands' natural tendency to recoil into fibrils (Fig. 6). Those gelatin fibrils showed a well-known banded pattern with a periodicity of $64\,nm$ similar to the collagen fibril[106]. The theory of determining the mesh size, $\xi_0 = (k_bT_\infty/G)^{1/3}$ (where, k_b is the Boltzmann constant) based on the rubber elasticity[107] underestimated the mesh size observed by Marmorat et al. (2016). MacKintosh et al. (1995) identified that the *semi-flexible network* shows increased rigidity due to its secondary structure between the crosslinks and must be taken into consideration to determine the mesh size[108]. Considering the network consists of effective spring where effective spring constant is k_{ef}, then the small strain shear modulus is related to the mesh size as[62],

$$\xi_0 = \frac{k_{ef}}{G} \tag{13}$$

For small strain, the rigidity arises from the straightening of α angle of the gelatin strand at the crosslink. However, Gelatin fibril will deform as well for large strain, and the large deformation of the fibril will be considered in later sections for the bubble growth. From Fig. 6, for any force (F) applied to the crosslink with effective spring constant (k_{ef}) will have two components; i) F_1 will stretch the gelatin strand with stretching spring constant k_1, and ii) torque τ will act to change angle α with angular deformation constant k_α. Treloar (1960) calculated the k_{ef} for polymeric chain and will be adopted here[109],

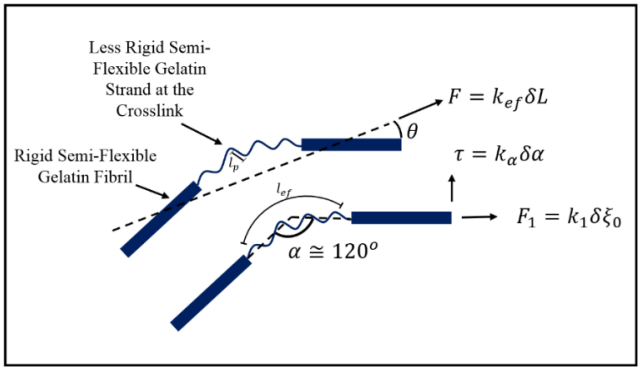

Fig. 6 Typical crosslink of the gelatin fiber network. Individual fibers (think blue line) are crosslinked via the gelatin strand (thin blue line).

$$\frac{1}{k_{ef}} = \frac{\delta L}{F} = n\left[\frac{cos^2(\alpha/2)}{k_1} + \frac{l_p^2 sin^2(\alpha/2)}{k_\alpha}\right] \tag{14}$$

In the above equation, $n = l_{ef}/l_p$, is the amount of zigzag, which is defined as the ratio of the effective length of the gelatin strand (l_{ef}) at the crosslink and the persistence length of the gelatin strand (l_p). The cryo-SEM observation showed that the statistical average crosslink angle is $\langle\alpha\rangle \cong 120^o$, hence $\langle sin^2\left(\frac{\alpha}{2}\right)\rangle = 0.75$ [62]. Considering crosslink deformation dominated by k_α for small strain and for an inextensible gelatin strand ($k_1 \gg k_\alpha$), we can drop the first term in Eq. (14),

$$k_{ef} = \frac{k_\alpha}{nl_p^2\langle sin^2\left(\frac{\alpha}{2}\right)\rangle} \tag{15}$$

From Treloar (1960) and Marmorat (2016), the angular deformation constant is related to the persistence length and length of the bond along the polymer backbone (l_0) as $k_\alpha = k_BT_\infty l_p/l_0$ [62,109]. Therefore, the effective spring constant is,

$$k_{ef} = \frac{4k_BT_\infty}{l_0 l_{ef}\langle sin^2\left(\frac{\alpha}{2}\right)\rangle} \tag{16}$$

There exist two limiting cases for the effective length (l_{ef}) of the gelatin strand (Fig. 6). For high-density crosslink, the gelatin strand will not be able to recoil to form a superstructure. Therefore, fibers will be made of gelatin strand only, and the effective length will be, $l_{ef} \to \xi_0/2$. On the other hand, for low-density crosslinks, fibers will have enough strands to recoil, and gelatin fibril with superstructure will form. Hence, the minimum gelatin strand effective length at the crosslink, which straightens in the small strain, will be reduced. In that case, since the theoretical minimum length would be two persistence length to form the crosslink bend, the effective length would be, $l_{ef} \to 2l_p$. From Eq. (13) and Eq. (16),

$$\xi_0 = \sqrt{\frac{8k_BT_\infty}{Gl_0\langle sin^2\left(\frac{\alpha}{2}\right)\rangle}} \quad for\ l_{ef} \to \xi_0/2 \tag{17}$$

$$\xi_0 = \frac{2k_BT_\infty}{Gl_0l_p\langle sin^2\left(\frac{\alpha}{2}\right)\rangle} \quad for\ l_{ef} \to 2l_p \tag{18}$$

Eq. (17) and Eq. (18) is the theoretical minimum and maximum limit of the fiber length, respectively [62]. The small strain shear modulus is measured for 5, 7, and 14% [w/v] of Knox gelatin gels using a piezoelectric cantilever measurement technique and reported in Fig. 7a from the ref.[110]. The black dashed line shows a linear fit with $R^2 = 0.99$. The shear modulus value is used in Eq. (17) and Eq. (18), and the mesh size is plotted in Fig. 7b. The arithmetic mean of one C-C bond and two C-N bonds is used as the bond length along the polymer backbone ($l_0 = 1.4$ Å) and persistence length ($l_p = 2.7\ nm$) for gelatin strand is used, respectively from the ref. [111] and [112]. The theory is validated by observing the SEM image of 3 different concentrations of gelatin gels. The SEM images are given in Fig. 7c, and the measurement of the mesh sizes of 3, 5, and 7% [w/v] gelatin gels are plotted in Fig. 7b and compared with Eq. (17) and Eq. (18). It seems the limiting case for Eq. (18) is valid, which means gelatin fibrils with the supramolecular structure are formed, and the gelatin strands connect the crosslinks.

The pore size is then measured using the Diameterj plugin with Fiji (Imagej2) software [113,114]. Each gel sample is cut with 0.2-micron thickness. We took images of 8 cuts for each gel concentration. The SEM image is first converted to an 8-bit binary image and then segmented using 16 different algorithms provided by the Diameterj. Therefore, a total of 8*16=128 images are averaged for each gel concentrations. Fig. 8 shows an 8-bit SEM image, segmented image, and pore size measurement for 3% gel as an example. The detailed procedure is described in the supplemental document.

Fig. 9 shows the pore size (A_p), and since ImageJ fits the pore size in an ellipse, we have shown the minor axis length (L_{MA}) of the pores in Fig. 10. As we have postulated in the previous section, a bubble nucleus of the critical radius (R_0) must be accommodated within a pore to cavitate under the tensile nucleation pressure (P_{nuc}). The maximum size of a sphere that can fit in an ellipse must have a radius that is half of the minor axis length. Therefore, in Eq. (10), we will use $R_0 \to L_{MA}/2$ for gel system to compute P_{nuc}.

Unit Cell Model and Mechanical Properties of Fibril

Since $l_{ef} \to 2l_p \ll \xi_0$, we will assume that the crosslink to crosslink fiber is consists of the gelatin fibril only. From now on, we will use gelatin fibril length and mesh size interchangeably. To construct the gelatin network, we will replace the contribution of the gelatin strand with torsional spring at the crosslink with effective torsional spring constant, K_t (Fig. 12).

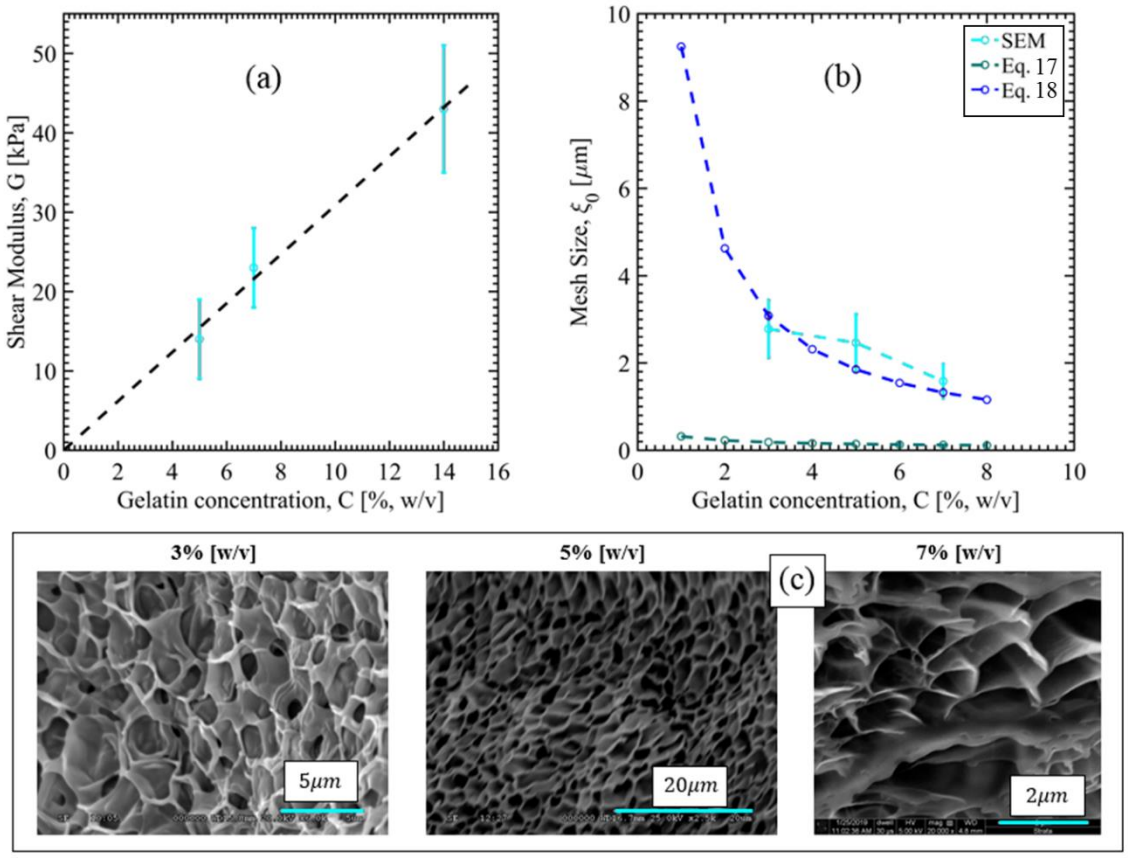

Fig. 7 (a) Shear modulus, (b) fiber length observed from the SEM images and theoretical model (Eq. (17) and (18)) fit, and (c) SEM images of different gel concentrations. The vertical red error bar indicates the standard deviation.

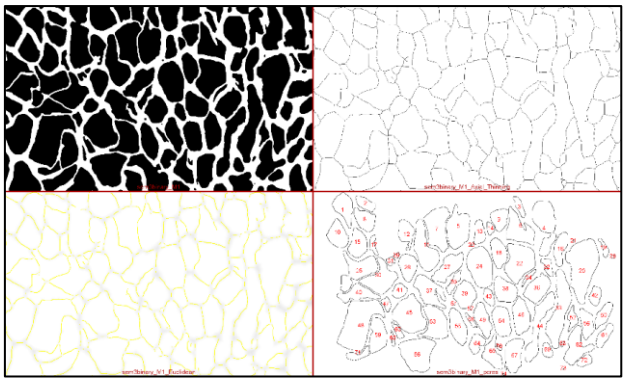

Fig. 8 8-bit image of the SEM image of 3% gel (top left). Segmentation is done in two steps (top right and bottom left). Pore count and size measurement are shown (bottom right).

Since gelatin triple-helical strands self-assemble into the secondary supramolecular structure as collagen fibril, which is modeled as semi-flexible fiber, we can model each gelatin fibril as such[82]. We used the word *fibril* for gelatin fiber to be consistent with the definition of the hierarchical structure of collagen micro-fibril, fibril, and fiber[115]. A semi-flexible fibril is defined such that its thermal persistence length is comparable to the fibril length, $L_P/\xi_0 \sim 1$. The persistence length of the gelatin fibril can be defined as the ratio between the bending rigidity and thermal energy, $L_P = E_f I_f / k_B T_\infty$, where E_f is the fibril Young's modulus and $I_f = \pi {d_f}^4/64$ is the area moment of inertia of the fibril, respectively. The material and geometric properties we need to compute the strain energy of the network are the fibril Young's modulus (E_f), crosslink torsional spring constant (K_t), fibril length (ξ_0), and diameter of the fibril (d_f). Considering the gelatin fibril as elastic beam which resists stretching and bending, and crosslink as torsional spring, the strain energy of the network for any given configuration is defined as [82],

$$U = U_S + U_B + U_T \tag{19a}$$

$$= \sum_{i=1}^{N_s} \left(\int_0^{\Delta\xi_0} F_f d\Delta\xi_0 \right)_i + \sum_{i=1}^{N_b} \left(\int_0^{\xi_0} \frac{M^2}{2E_f I_f} dx_f \right)_i + \sum_{j=1}^{N_t} \left(K_t \frac{\Delta {\theta_t}^2}{2} \right)_j \tag{19b}$$

In Eq. (19b), N_s and N_b are the number of fibrils that contribute to the stretching strain energy (U_S) and bending strain energy (U_B), respectively. Crosslink torsional strain energy (U_T) is due to the N_t number of crosslinks having rotational angles θ_t. The difference between the current and reference configuration is indicated by Δ, and $A_f = \pi {d_f}^2/4$ is the cross-sectional area of the fibrils. The stretching force is defined as, $F_f = E_f A_f (\exp(B_f \varepsilon_f) - 1)/B_f$, where B_f is a material parameter, and the Green strain (ε_f) is calculated using the fibril stretching ratio as, $\varepsilon_f = ({\lambda_f}^2 - 1)/2$ [116]. M is the non-uniform (fibril lengthwise) transverse moment on the fibril due to bending (x_f is the fibril local longitudinal coordinate defined in Fig. 17).

Incorporating the bubble growth ratio (λ_B) into Eq. (19), we can compute the strain energy of the network. Ultimately, we will assume that the network failure strain energy is the work done by P_{RFN}. In the next sub-section, we will adopt a unit cell model

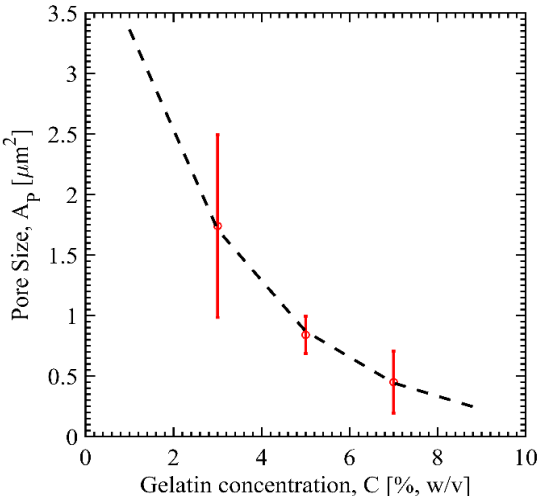

Fig. 9 Pore area size was measured by observing the SEM image of different gel concentrations. (Vertical red error bar indicates the standard deviation)

to find fibril material and geometric properties. Then we will incorporate the bubble growth into Eq. (19).

In the unit cell model, we will fit the macroscale stress-strain data to the unit cell's microstructural deformation. For large strain, gelatin gel is proposed to behave like incompressible hyperelastic Ogden material[117]. The strain energy density function for the first order Ogden material in terms of principal stretches of gel (λ_{Gi}) in three coordinate directions ($i = 1,2,3$) is,

$$W_G = \frac{\mu_G}{\beta} (\lambda_{G1}^\beta + \lambda_{G2}^\beta + \lambda_{G3}^\beta - 3) \tag{20}$$

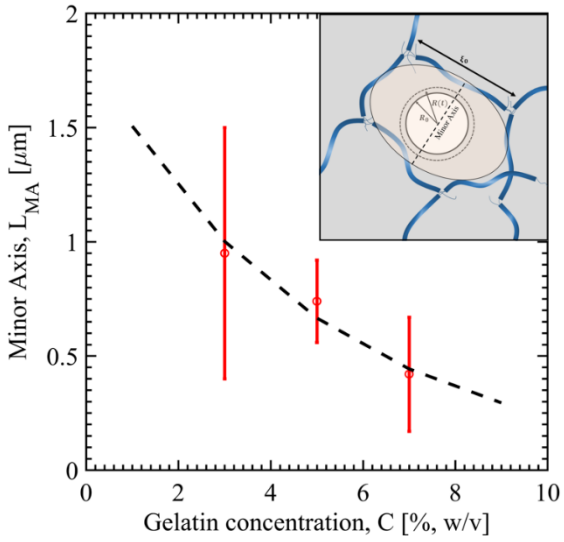

Fig. 10 Minor axis length of the pore area. (Vertical red error bar indicates the standard deviation)

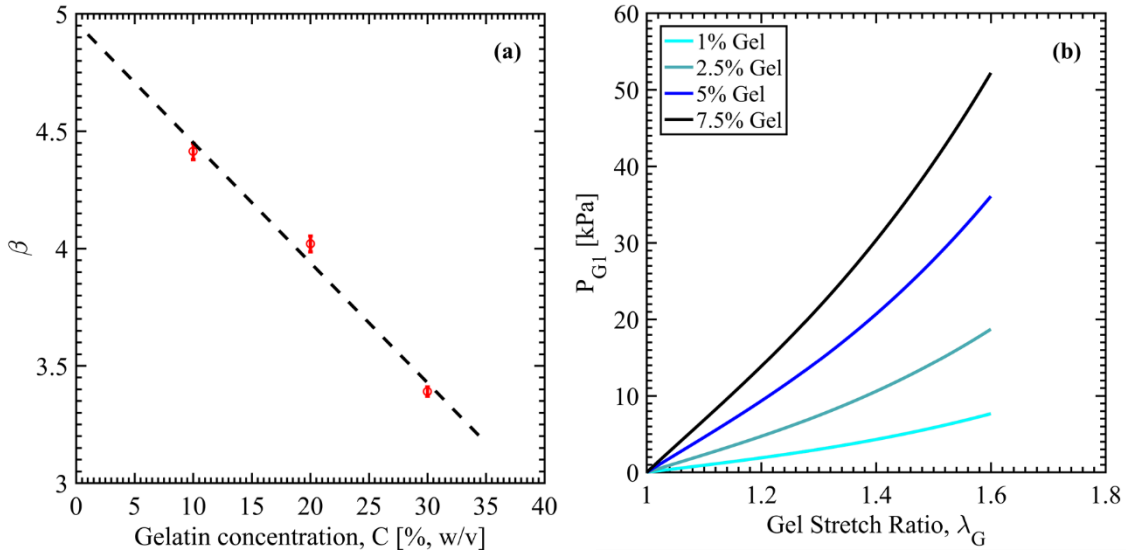

Fig. 11 (a) Strain hardening parameter (β) for gelatin from uniaxial testing[117]. (b) The First Piola-Kirchhoff stress of gelatin gel as a function of the gel stretch (Eq. (23)).

Where μ_G and β are material properties. Particularly β is the strain hardening parameter, and for gelatin, β is reported from ref [117] (plotted in Fig. 11a). The small strain shear modulus is defined as, $G = \mu_G\beta/2$, and given in Fig. 7a. For uniaxial tension, the deformation gradient tensor $\boldsymbol{F_G}$ is,

$$\boldsymbol{F_G} = \begin{bmatrix} \lambda_{G1} & 0 & 0 \\ 0 & \lambda_{G2} & 0 \\ 0 & 0 & \lambda_{G3} \end{bmatrix} \tag{21}$$

The incompressibility condition is met when $\det(\boldsymbol{F_G}) = \lambda_{G1}\lambda_{G2}\lambda_{G3} = 1$. For uniaxial tension in direction 1, let $\lambda_{G1} = \lambda_G$ and $\lambda_{G2} = \lambda_{G3} = \lambda_G^*$, then from incompressibility condition, $\lambda_G^* = 1/\sqrt{\lambda_G}$. The three principal values of the Cauchy stress ($\boldsymbol{T_G}$) is defined as,

$$T_{Gi} = -\tilde{p} + \lambda_{Gi}\frac{\partial W_G}{\partial \lambda_{Gi}} \tag{22}$$

Where $\tilde{p}$ is the pseudo-pressure term that is determined for uniaxial tension by setting, $T_{G2} = T_{G3} = 0$. The experimental data reported in ref [117] is for the first Piola-Kirchhoff (nominal) stress, which is defined as, $\boldsymbol{P_G} = det(\boldsymbol{F_G})\boldsymbol{T_G}(\boldsymbol{F_G}^T)^{-1}$. Therefore, the first Piola-Kirchhoff stress in direction 1 is (plotted in Fig. 11b),

$$P_{G1} = \frac{2G}{\beta}\left(\lambda_G^{(\beta-1)} - \lambda_G^{(-\frac{\beta}{2}-1)}\right) \tag{23}$$

The three-dimensional microstructure of the gel system is represented by the unit cell in Fig. 12a. The proposed unit cell assumes isotropic microstructure, and the angles are set to be $\psi = 45°$and $\phi = 35.26°$ for the unit cell to be symmetric in all principal coordinate directions[77]. The other two geometric properties are fibril diameter (d_f) and length (ξ_0). The initial dimensions of the unit cell in three coordinate directions are,

$$L_{1,0} = 2\xi_0(1 + cos\phi cos\psi) \tag{24a}$$

$$L_{2,0} = 2\xi_0(1 + sin\phi) \tag{24b}$$

$$L_{3,0} = 2\xi_0(1 + cos\phi sin\psi) \tag{24c}$$

Previously, we have assumed that the small strain is due to the strengthening of the crosslink angles. Therefore, oblique fibrils

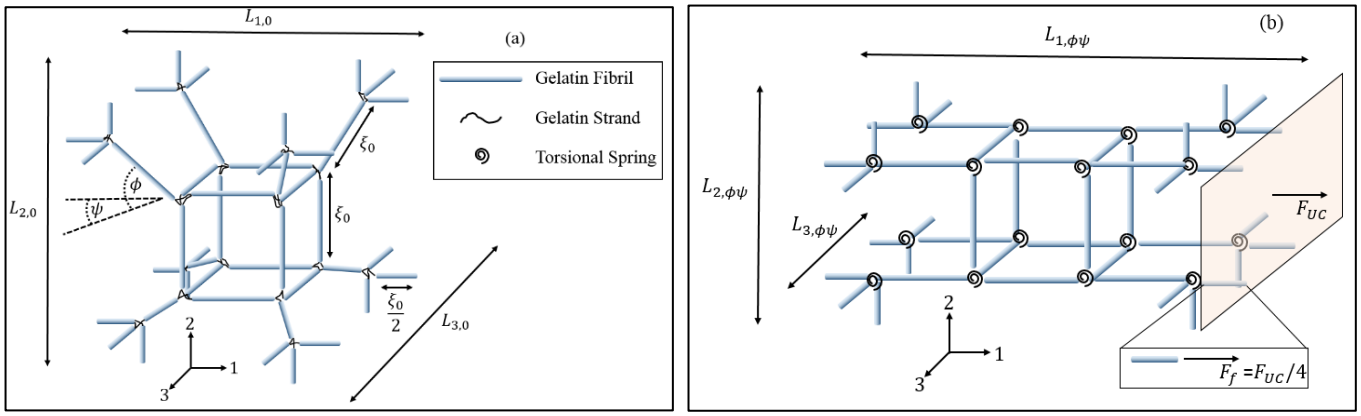

Fig. 12 (a) A representative unit cell of the random fiber network of gelatin gel. (b) Uniaxial stretching until fibers align in the stretch direction due to the crosslink rotation.

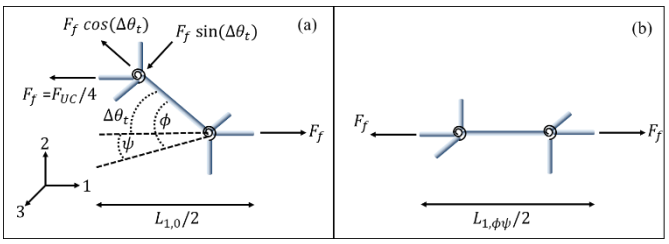

Fig. 13 (a) one oblique fiber is shown at the beginning of the uniaxial tension. The strain energy stored until the fibers align in the stretching direction is due to the crosslink's rotational strain energy. (b) fibers alignment is completed, and further stretching of the fiber stores energy due to stretching only.

are aligned parallel to direction 1 before fibril level stretch (λ_f) imposed on the fibrils (Fig. 12b). The dimension of the unit cell when fibril alignment occurs are,

$$L_{1,\phi\psi} = 4\xi_0 \tag{25a}$$

$$L_{2,\phi\psi} = 2\xi_0 \tag{25b}$$

$$L_{3,\phi\psi} = 2\xi_0 \tag{25c}$$

The gel stretch is defined as,

$$\lambda_G = \frac{L_1}{L_{1,0}} \tag{26}$$

In the current configuration, the dimension of the unit cell in direction 1 is L_1. The gel stretch at the fibril alignment is,

$$\lambda_{G,align} = \frac{L_{1,\phi\psi}}{L_{1,0}} \tag{27}$$

Since fibril stretch occurs after fibril alignment, the fibril stretch is defined as,

$$\lambda_f = \frac{L_1}{L_{1,\phi\psi}} = \frac{\lambda_G}{\lambda_{G,align}} \qquad for\ \lambda_G \geq \lambda_{G,align} \tag{28}$$

The first Piola-Kirchhoff stress is defined as the force per initial unit area. Therefore, the force on the unit cell (F_{UC}) is,

$$P_{G1} = \frac{F_{UC}}{L_{2,0}L_{3,0}} \tag{29}$$

From Fig. 13a, the force on the fibril (F_f) is one-fourth of the force on the unit cell, $F_f = F_{UC}/4$. From Eq. (19b), we can decompose the stored strain energy of the RFN as crosslink deformation and fiber stretching (Fig. 13a and 13b),

$$U_T = \sum_{j=1}^{N_t=16} K_t \frac{{\Delta\theta_t}^2}{2} \qquad for\ \lambda_G \leq \lambda_{G,align} \tag{30a}$$

$$W_G(\lambda_G)V_U = U_S = \sum_{i=1}^{N_s=4} \left(\int_0^{\Delta\xi_0} F_f d\Delta\xi_0 \right)_i - U_T(\lambda_{G,align}) \qquad for\ \lambda_G > \lambda_{G,align} \tag{30b}$$

Where unit cell volume is $V_U = L_{1,0}L_{2,0}L_{3,0}$. Due to the symmetry, only one oblique fibril is shown in Fig. 13. The strain energy in Eq. (30a) is due to the rotation of the 16 crosslinks ($N_t = 16$) until $\lambda_{G,align}$, followed by four fibrils ($N_s = 4$) stretching until gel failure stretch, ${\lambda_G}^u$ (Fig. 13). K_t and E_f, $d_f$and B_f will be computed from Eq. (30a) and (30b) using nonlinear regression analysis, respectively. 60% strain (${\lambda_G}^u = 1.6$) is taken to be the failure criterion for the gelatin gels reported in ref. [117]. A similar failure strain is reported for collagen gels as well [82,118]. Therefore, the fibril level stretch is computed from Eq. (28), which is $\lambda_f = 1.26$. Collagen fibril yield strain and ultimate failure strain are reported to vary between 10-32% and 35-45% strain, respectively [119]. Baumberger et al. (2006) observed that the fiber network failed by crosslink disentanglement at a low deformation rate and suggested that a higher strain rate network fails due to individual fiber scission [61]. Therefore, in the uniaxial testing at the quasi-static stretching, we can conclude that gel fails via crosslink failure,

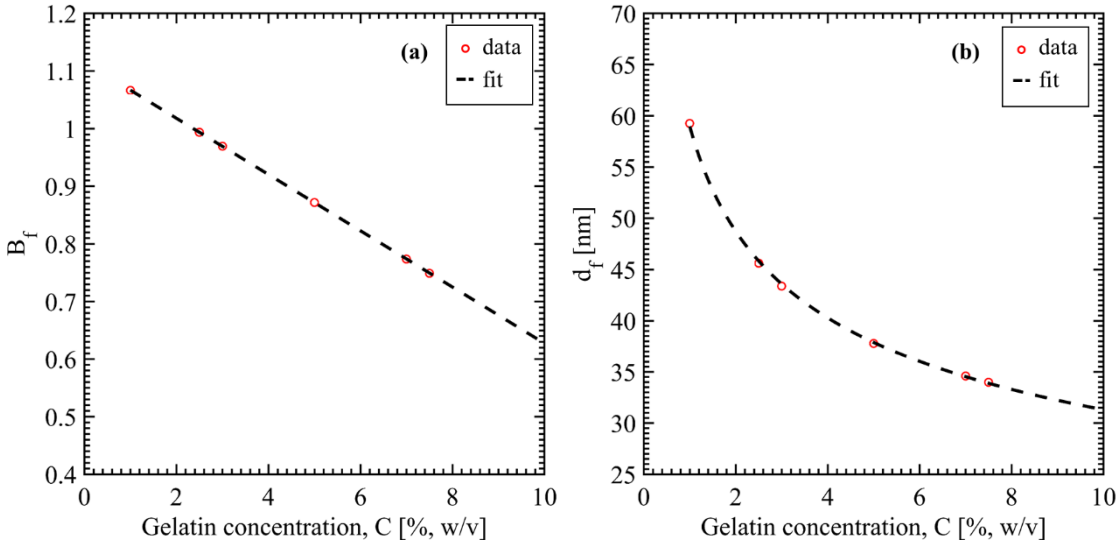

Fig. 14 (a) Nonlinear material parameter, and (b) diameter of the fibers are shown for different gel concentrations.

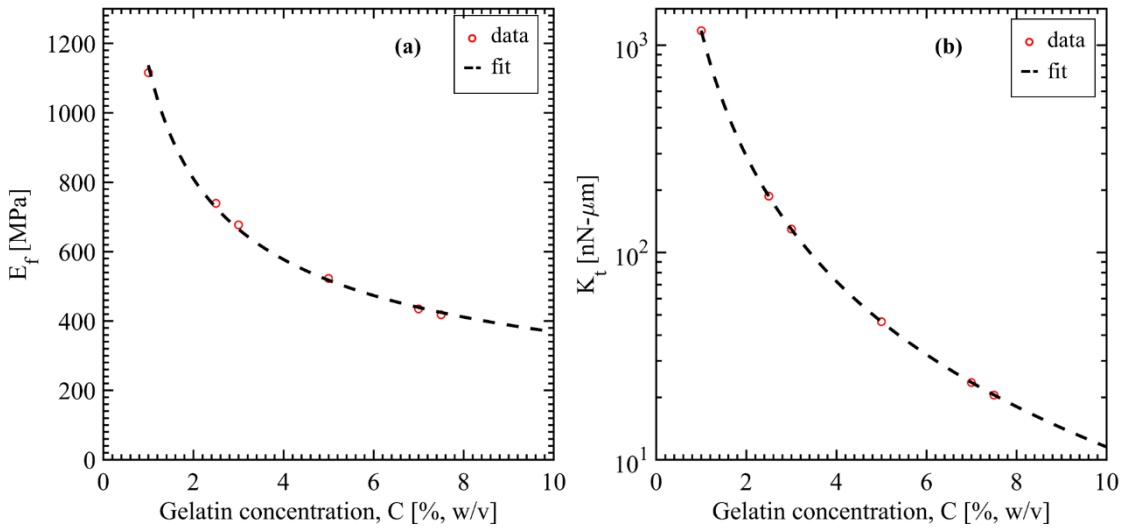

Fig. 15 (a) Young's modulus of the fiber, and (b) crosslink torsional constant of the network as shown for different gel concentrations.

and fiber does not attain its failure strain. However, bubble growth imposes high strain rate deformation in the surrounding medium, and we will assume that fiber failure strain (35-45%) is the primary failure mechanism for bubble growth.

There are several studies where collagen fiber properties are measured by uniaxial stress-strain testing. However, we have not found any material property for gelatin fibril to the best of our knowledge. Therefore, the unit cell model is developed, which can be utilized to estimate the gelatin fibril properties as the model can relate gel level properties to fibril level properties in close form. Since gelatin fibril and collagen fibril are similar in their supramolecular structure, we can use collagen fibril properties as a guideline. Susilo et al. (2010) have summarized the literature on collagen properties in detail, and readers are referred to that for further reading [77]. We have found that the collagen fiber properties vary in a wide range of magnitude. One of the main reasons for this wide range is the hierarchical structure of collagen fiber (e.g., microfibril, fibril, and fiber). Diameter is one of the parameters that can distinguish the collagen fibril from the collagen fiber. Collagen fibril is said to have a diameter ranging from 20 nm to 400 nm, while collagen fiber may have a diameter greater than 400 nm [120–122]. Fig. 14 plotted the gelatin fibril diameter for different concentrations using the unit cell model. The diameter range varies from 31 to 58 nm and well within the discussed range given above. The decreasing trend of the diameter is because the crosslink density increases with increasing concentration; therefore, there are fewer gelatin strands to recoil to form thicker fibrils. Cryo-SEM observation of increasing crosslink density showed a similar trend [62].

The range mentioned above for collagen fibril diameter (20 to 400 nm) corresponds to fibril Young's modulus from 32 MPa to 11.5 GPa [123–125]. For collagen fiber ($d_f > 400nm$) the modulus range is given to vary between 1.8 MPa to 1.2 GPa [77]. Fig. 15 plotted the Young's modulus of gelatin fibril for different concentration of gelatin gel by utilizing the unit cell model and gel level material properties as described above. The Young's modulus range is shown to be within 400 MPa to 1.15 GPa and falls within the collagen fibril modulus range. The fibril parameters will be used in the next sub-section to quantify the network strain energy due to bubble growth.

Extra Tensile Pressure, ΔP_T: Network Failure Model

Network Strain Energy due to the Bubble Growth

The network strain energy formulation shown in Eq. (19b) can be utilized if we can establish correlations between the bubble growth ratio (λ_B) and three strain energy parameters, i.e. $\Delta\xi_o$, M and $\Delta\theta_t$. However, Eq. (19b) is the superposition of three different modes of deformations (e.g., stretching, bending, and torsion). We will correlate the bubble growth to each mode of deformation separately. In doing so, a unit cell of the gelatin network is shown in Fig. 16a, enclosing a bubble of radius R_0. Considering in a strain-free reference configuration, we assume the bubble center lies at the origin of a spherical coordinate whose radius is R_0. In the current configuration at the time t, the bubble radius is $R(t)$. Any material points initially at $\boldsymbol{x_0} = \rho_0 \boldsymbol{e}_\rho$ will be at $\boldsymbol{x} = \rho \boldsymbol{e}_\rho$ in the current configuration. The deformation gradient tensor of the surrounding medium due to bubble growth is [51],

$$\boldsymbol{F_B} = \begin{bmatrix} \frac{\partial \rho}{\partial \rho_0} & 0 & 0 \\ 0 & \frac{\rho}{\rho_0} & 0 \\ 0 & 0 & \frac{\rho}{\rho_0} \end{bmatrix} \tag{31}$$

The condition of incompressibility of the medium requires that $\det(\boldsymbol{F_B}) = 1$. Therefore, from Eq. (31), the radial stretch is, $\frac{\partial \rho}{\partial \rho_0} = (\frac{\rho_0}{\rho})^2$. Since $\rho_0 < \rho$ while bubble grows, the radial stretch decreases monotonically as a function of radial distance. Hence, in Fig. 16b, we have shown that all the oblique and end fibrils will experience buckling (only one corner is shown due to the ease of representation) except the fibril in the cubic portion

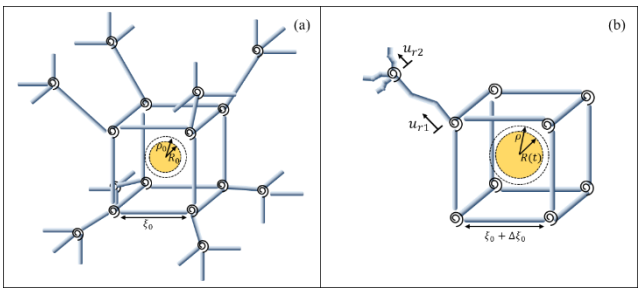

Fig. 16 (a) Bubble nucleus enclosed by the unit cell. (b) bubble growth causing fibril stretching (cubic part) and buckling (oblique fibril).

of the unit cell. However, the buckling of semi-flexible filament is entropy dominant [49]. Since the strain energy formulation in Eq. (19b) assumes the negligible entropic contribution, we will only consider the cubic portion of the unit cell that will contribute to the strain energy, and buckled fibrils are omitted.

Fibril Stretching Strain Energy

In Fig. 16b, we have shown only the mode-I (stretching) deformation of the cubic cell. At the reference configuration, the initial volume of the liquid phase within the cubic cell is (from Fig. 16a),

$$V_0 = \xi_0^3 - \frac{4}{3}\pi R_0^3 \tag{32}$$

Now, after an infinitesimal time increment, the bubble grows to $R(t)$ and displaces the surrounding liquid, which eventually interacts with the network and increases the fiber length to $\xi_0 + \Delta\xi_0$. The volume of the surrounding liquid within the displaced cubic cell is.

$$V = (\xi_0 + \Delta\xi_0)^3 - \frac{4}{3}\pi R^3 \tag{33}$$

Assuming incompressibility of the liquid phase ($V_0 = V$), we can equate Eq. (32) and Eq. (33) to establish the correlation between the incremental fibril length, $\Delta\xi_0$ and the bubble extension ratio, λ_B as,

$$\Delta\xi_0 = \frac{4}{9}\frac{\pi R_0^3}{\xi_0^2}({\lambda_B}^3 - 1) \tag{34}$$

The failure criterion for Eq. (34) is set to be, ${\Delta\xi_0}^u = \xi_0(\lambda_f^u - 1)$. The fibril failure stretch (λ_f^u) is varied between 1.35 to 1.45, as discussed in the previous section.

Fibril Bending and Crosslink Torsional Strain Energy

Since the liquid phase is displaced radially outward in all directions, we can simplify the fibrils' bending shape and the crosslink rotation. From Fig. 17a, looking upon a cross-sectional view of the cubic cell cutting by the *A-A plane*, we can superimpose a circle of radius, $R_{AA} = \sqrt{3}\xi_0/2$ on the fibril deformation due to bending. Geometric similarity requires that on the *A-A plane,* the fractional area of the bubble growth (green shade) is related to the area (A_2) under the bent fibril (Fig. 17b). A deflection function ($y(x_f)$) is assumed for the fibril considering a simply supported beam with a constant distributed load per unit length (q) with local fibril coordinate system (x_f, y_f) is defined as well (Fig. 17c). The moment on the fibril is then defined as,

$$M = E_f I_f \frac{d^2y}{{dx_f}^2} = \frac{qx_f}{2}(x_f - \xi_0) \tag{35}$$

The first derivative of the deflection function evaluated at either end of the fibril ($x_f = 0\ or\ \xi_0$) gives,

$$\Delta\theta_t = \frac{q{\xi_0}^3}{24E_f I_f} \tag{36}$$

Since the area under the deflected fibril is,

$$A_2 = \int_0^{\xi_0} y dx_f = 0.207\pi R_o^2(\lambda_B^2 - 1) \tag{37}$$

Therefore, the distributed load on the fibril can be related to the bubble growth as,

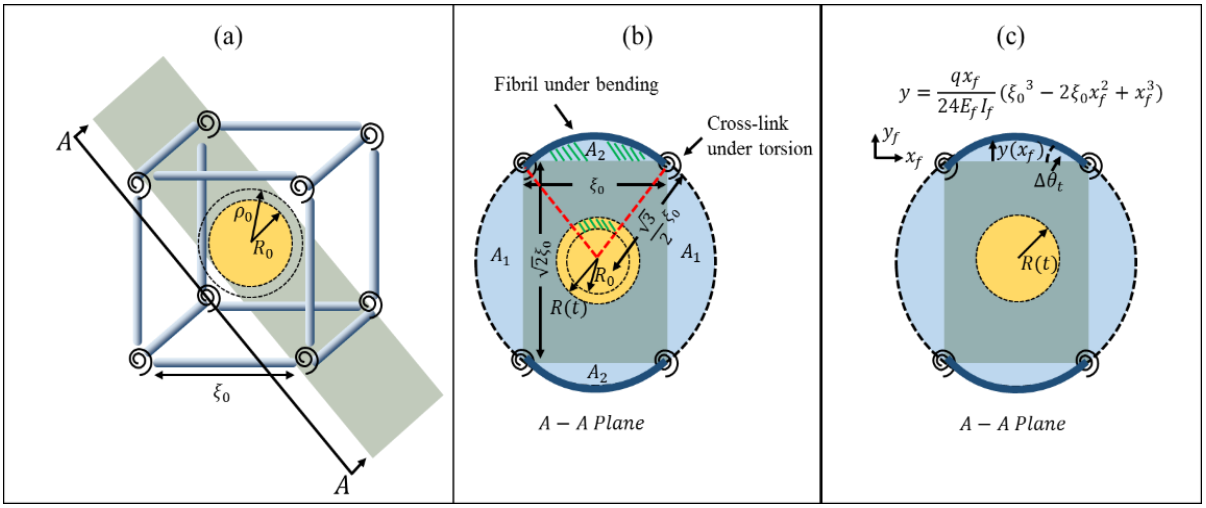

Fig. 17 (a) a diagonal plane (A-A) is shown on which fibril bending occurs due to the bubble growth. (b) and (c) projection on the A-A plane showing geometric relation of bubble growth area and fiber bending.

$$q = \frac{24.84\pi}{\xi_o^5} E_f I_f R_o^2 (\lambda_B^2 - 1) \quad (38)$$

Eq. (34), (35), (36), and (38) will be used with Eq. (19b) to compute the network strain energy due to bubble growth until fibrils failed at λ_f^u.

Extra Tensile Pressure

Now that we have formulated the strain energy stored in the network due to the bubble growth, we can define the pressure contribution from the strain energy per unit volume as,

$$P_{RFN} = \frac{U_{cric}}{\Delta V_{cric}} \quad (39)$$

In the above equation, $U_{cric} = U(\lambda_f^u)$ from Eq. (19). $\Delta V_{cric} = V_U - V_B^u$ is the difference between the volume of the unit cell and the volume of the growing bubble. The bubble volume is defined as,

$$V_B = \frac{4}{3}\pi R_o^3 (\lambda_B^3 - 1) \quad (40)$$

At the critical condition, $V_B^u = V_B(\lambda_B^u)$. The fibril failure stretch, and bubble failure stretch are related through Eq. (34) as,

$$\lambda_f^u = 1 + \frac{4}{9}\frac{\pi R_o^3}{\xi_o^3}({\lambda_B^u}^3 - 1) \quad (41)$$

Therefore, from Eq. (12), the extra tensile pressure is,

$$\Delta P_T = P_v \left(\frac{1}{\lambda_B^u}\right)^3 - \frac{2S}{R_o \lambda_B^u} - \frac{U_{cric}}{\Delta V_{cric}} \quad (42)$$

In the next section, we will develop the necessary formulation to quantify the extra tensile pressure based on the fracture theory.

Extra Tensile Pressure, ΔP_T: Fracture Model

In the previous section, we have formulated the extra tensile pressure criteria based on the failure of the RFN of the gel system. This section will use the well-known Griffith's criterion for gelatin fracture due to bubble growth, considering gel as the homogeneous hyperelastic Ogden material. We know that elastic materials can store energy when deformed and return to their reference configuration by spending that stored energy upon withdrawal of the loading. However, there is a limit on the stored energy beyond which fracture initiates and materials fail. Griffith's theorem states that a crack will propagate when surface energy is exceeded by the energy released due to new crack growth [13,126]. The critical energy release rate (G_c) is the material property that is used as the criterion for the material to resist fracture. Wire cutting tests are done to estimate G_c for gelatin gel and reported in Fig. 18 from ref. [61,117,127].

Several authors have modified the Rayleigh-Plesset equation of bubble dynamics for viscoelastic materials. The elastic term is added for linear Hookean, nonlinear Neo-Hookean, and strain hardening Fung models [1,51,128]. They have provided the procedure in detail, and readers are referred to them for further study. However, in this manuscript, we will develop the elastic contribution for the Ogden material model.

From Eq. (31), the deformation gradient tensor of the surrounding medium in spherical coordinate direction ($i = \rho, \theta, \varphi$) is,

$$\boldsymbol{F_B} = \begin{bmatrix} \lambda_{B,\rho\rho} & 0 & 0 \\ 0 & \lambda_{B,\theta\theta} & 0 \\ 0 & 0 & \lambda_{B,\varphi\varphi} \end{bmatrix} = \begin{bmatrix} \frac{\partial \rho}{\partial \rho_0} & 0 & 0 \\ 0 & \frac{\rho}{\rho_0} & 0 \\ 0 & 0 & \frac{\rho}{\rho_0} \end{bmatrix} \quad (43)$$

The incompressibility condition is applicable here as well, which requires,

$$\frac{\partial \rho}{\partial \rho_0} = \left(\frac{\rho_0}{\rho}\right)^2 \quad (44)$$

Integrating the above equation and setting boundary condition at the bubble wall, $\rho = R(t)$ we get the reference coordinate in terms of the current coordinate of the material point,

$$\rho_0 = (\rho^3 - R(t)^3 + R_0^3)^{\frac{1}{3}} \quad (45)$$

From Eq. (22), the Cauchy stress tensor is,

$$\boldsymbol{T_G} = \begin{bmatrix} -\tilde{p} + \frac{2G}{\beta}\left(\frac{\rho_0}{\rho}\right)^{2\beta} & 0 & 0 \\ 0 & -\tilde{p} + \frac{2G}{\beta}\left(\frac{\rho}{\rho_0}\right)^{\beta} & 0 \\ 0 & 0 & -\tilde{p} + \frac{2G}{\beta}\left(\frac{\rho}{\rho_0}\right)^{\beta} \end{bmatrix} \quad (46)$$

In the above equation, we used $\lambda_{B,i}$ from Eq. (43) for the partial derivative of the strain energy density function. The pseudo-pressure term ($\tilde{p}$) in Eq. (22) and Eq. (46) is related to the hydrostatic pressure (p) as [1,51],

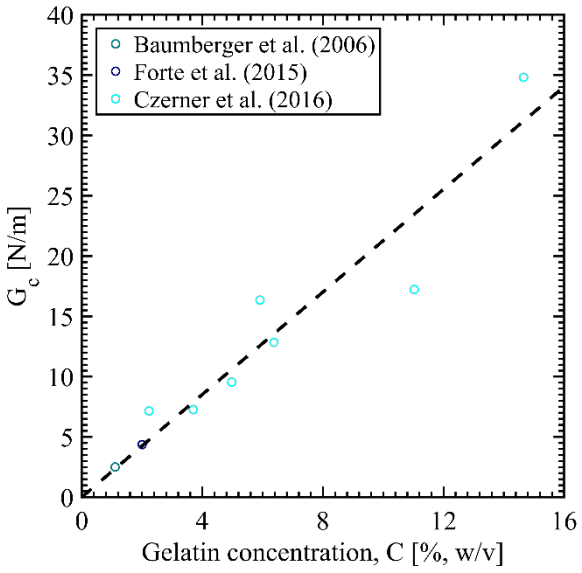

Fig. 18 Critical energy release rate as a function of the gelatin concentration.

$$p = -\frac{T_{G,\rho\rho} + T_{G,\theta\theta} + T_{G,\phi\phi}}{3}$$

$$= \tilde{p} - \frac{2G}{3\beta}\left[\left(\frac{\rho_0}{\rho}\right)^{2\beta} + 2\left(\frac{\rho}{\rho_0}\right)^{\beta}\right] \quad (47)$$

Finally, the elastic contribution to the bubble dynamics is found by integrating the momentum equation from the bubble wall, $\rho = R(t)$ to $\rho \to \infty$ [1,51,58,128],

$$\Sigma = \int_{R(t)}^{\infty} -\left[\frac{2T_{G,\rho\rho} - T_{G,\theta\theta} - T_{G,\phi\phi}}{\rho}\right] d\rho$$

$$= \int_{R(t)}^{\infty} -\frac{4G}{\beta}\left[\frac{{\rho_0}^{2\beta}}{\rho^{2\beta+1}} - \frac{\rho^{\beta-1}}{{\rho_0}^{\beta}}\right] d\rho \quad (48)$$

Setting $\gamma = \rho/\rho_0$ and using Eq. (45), we get,

$$d\gamma = \left(\frac{1}{\rho_0} - \frac{\rho^3}{\rho_0^4}\right) d\rho \quad (49)$$

Considering, $\lambda_{B,\theta\theta} = \lambda_{B,\varphi\varphi} = \lambda_B = R/R_0$, Eq. (48) becomes,

$$\Sigma = \int_{\lambda_B}^{1} -\frac{4G}{\beta}\left[\gamma^{-(2\beta+1)}\left(\frac{1-\gamma^{3\beta}}{1-\gamma^3}\right)\right] d\gamma \quad (50)$$

The above equation is integrated numerically using the quadrature theorem. The stored strain energy due to the elastic contribution is [1,38],

$$U_{\Sigma} = \int_{R_0}^{R} 4\pi\Sigma\rho^2\, d\rho \quad (51)$$

The energy release rate per unit crack area is defined as $\partial \mathrm{U}_{\Sigma}/\partial A_c$, where $A_c = \pi R^2$ is the crack area. Applying Griffith's criterion of fracture on the energy release rate we get,

$$-\left(\frac{\partial U_{\Sigma}}{\partial A_c}\right) \geq 2R_0 f(\lambda_B) \quad (52)$$

Where $f(\lambda_B)$ is (using two dummy variables $(\zeta, and\ \eta)$),

$$f(\lambda_B) = {\lambda_B}^4 \frac{\partial}{\partial\zeta}\left(\zeta^{-3}\int_1^{\zeta}\Sigma\eta^2 d\eta\right)\Big|_{\zeta=\lambda_B} \quad (53)$$

At the critical condition, bubble fracture stretch is defined as, ${\lambda_B}^u = R_u/R_0$. Therefore, Eq. (50) can be numerically integrated until the fracture stretch by setting $f({\lambda_B}^u) = G_c/2R_0$ to find ${\lambda_B}^u$. We can then use Eq. (51) to find the total fracture energy at failure,

$$U_{\Sigma_{cric}} = \int_{R_0}^{R_u} 4\pi\Sigma\rho^2\, d\rho \quad (54)$$

Therefore, the extra tensile pressure can be defined in terms of the total fracture energy per unit volume of the bubble growth as,

$$\Delta P_T = \frac{U_{\Sigma_{cric}}}{V_B^u} \quad (55)$$

Results and Discussion

Random Fiber Network

In developing the strain energy-based criterion for the onset of cavitation in soft materials, we have estimated the fibril and the network properties $(E_f, d_f, B_f, and\ K_t)$ from the gel level properties $(G\ and\ \beta)$ of the gelatin gels. The network's strain energy formulation considers fibrils as an elastic beam, and they store energy by stretching and bending. This elastic beam model is justified since the fibril's persistence length is much higher than the mesh size. Fig. 19 shows the fibril thermal persistence length and how it compares to the mesh size. Collagen fibers, having mesh size in the micrometer range ($\sim 2\mu m$) and thermal persistence length in the millimeter range ($\sim 10mm$), are often modeled as the elastic beam [82,83]. $L_P/\xi_o < 2/\pi^{3/2}$ and $L_P/\xi_o \gg 1$ correspond to *flexible* and *rigid rod* type fibers, respectively [49]. A flexible fiber's elastic response is due to the decrease in entropic conformation, and rigid rod-type fibers are modeled as beam theory. In between, there lies the definition of the *semi-flexible* fibers ($L_P/\xi_o \sim 1$) which shows elastic response by both stretching and bending. At low concentration and lower molecular weight, a semi-flexible fiber network shows *nonaffine* deformation, and fiber response is mainly due to bending. As concentration increases, the network tends to show more *affine* deformation dominated by fiber stretching [87]. In the crosslinked network such as gelatin hydrogel, the geometric persistence length is comparable to the mesh size, and fibers are considered semi-flexible.

Using Eq. (19), the network's strain energy for different gel concentrations is plotted in Fig. 20. To quantify the contribution of different modes of deformation, the critical values (see Eq. (39)) are reported for the initial bubble radius of $1.2\mu m$ and fiber failure strain is taken to be 40% ($\lambda_f^u = 1.40$). The total critical strain energy (U_{cric}) is due to the stretching (U_S) of the fibers, since both bending energy of the fiber (U_B) and crosslink rotational energy (U_T) are few orders of magnitude lower than the stretching energy. Although the bending energy

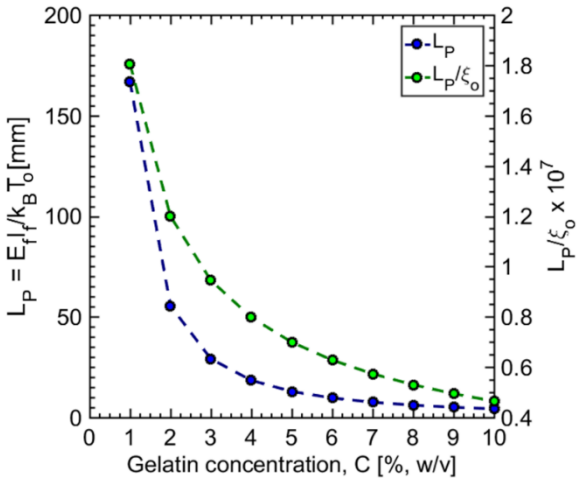

Fig. 19 The persistence length of the gelatin fibers is plotted on the left axis, based on the geometric (d_f) and mechanical (E_f) properties reported in Fig. 14 and Fig. 15, respectively. The ratio between the persistence length and mesh size (Fig. 7b) is plotted on the right axis. Both are shown as a function of the gel concentration.

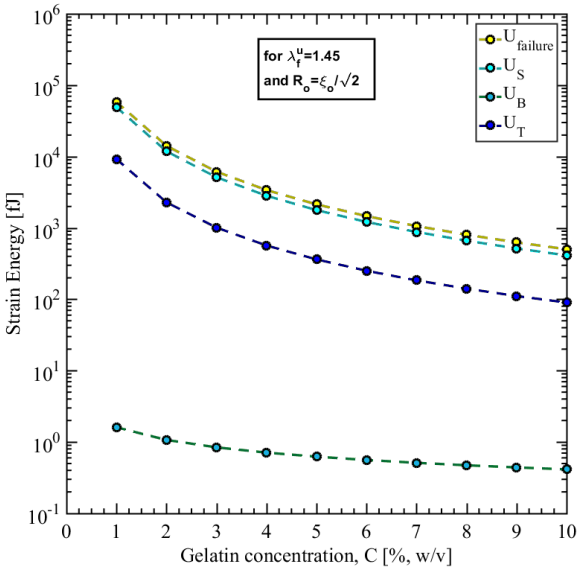

Fig. 20 The strain energy of the network due to the bubble growth from Eq. (19) corresponds to $R_o = 1.2\mu m$ and $\lambda_f^u = 1.40$.

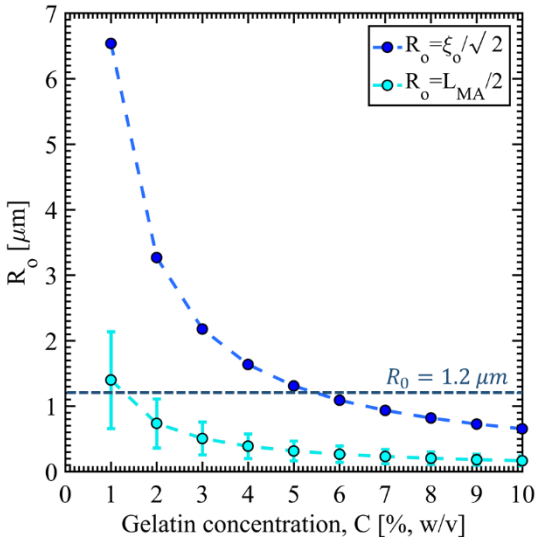

Fig. 21 Critical bubble radius based on the unit cell model and pore size from the SEM image.

contribution increases slightly for low concentration, the network deformation is mainly affine and stretching dominant.

Nucleation Pressure and Initial Bubble Radius

Fig. 21 plots the critical bubble size as a function of the gelatin gel concentration. The navy blue dotted line depicts the maximum bubble size that can be inscribed in the cubic portion of the unit cell model, which is half of the diagonal of the side face of the cube ($R_o = \xi_o/\sqrt{2}$). However, the network's SEM image observation indicates a much smaller *mean pore size* with a high standard deviation for low concentration (see Fig. 9 and 10). The maximum bubble size that can be formed within the network is then limited by the pore size (turquoise dotted line) and defined as half of the pores' minor axis length ($R_o = L_{MA}/2$). The nucleation formation energy in pure liquid corresponds to the critical nuclei size ($R_o \sim 1.2\ \mu m$) from experimental observation [59], and shown as the horizontal cobalt blue dotted line.

A random fiber network, having a large distribution of pore size, may have enough large pores where nucleation formation energy will only depend on the surface energy ($2S/R$). However, the surface tension (S) value depends on various factors, such as the gel states (solution or gel), temperature, interface curvature, liquid inter-molecule affinity in the presence of the gelatin network [105,129,130]. In Fig. 22a, we have shown the surface tension of gelatin gel, both in solution and gel states, and compared it with water surface tension ($S_{water} \sim 72 mN/m$) [59,131,132]. In the solution state, surface tension (S_{sol}) drops compared to the pure water while increases in the gel state (S_{gel}). The gelation process, however, starts by nonspecific hydrophobic interaction and the secondary supramolecular fibril forms [65]. As the network topology reaches

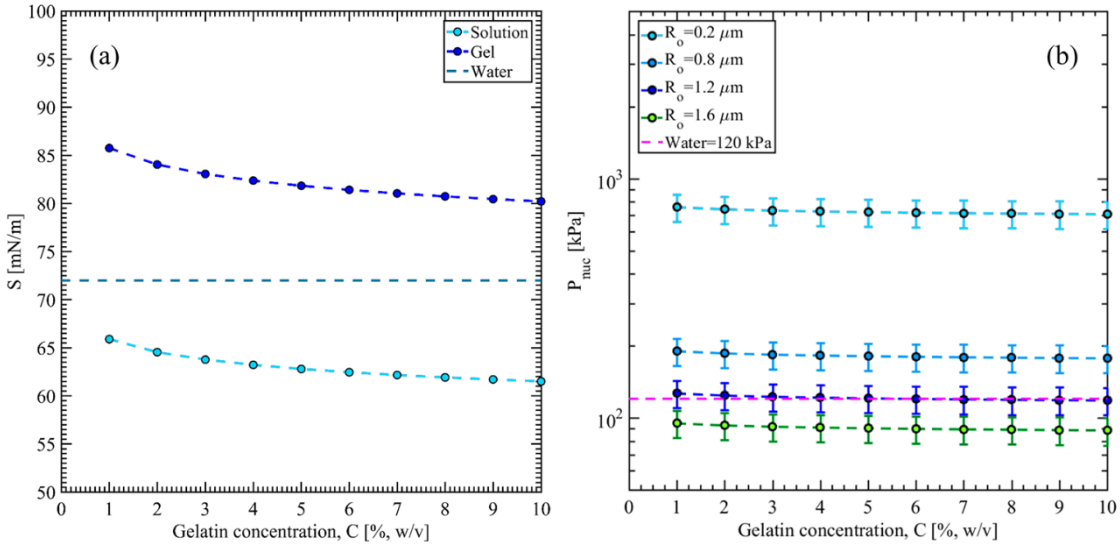

Fig. 22 (a) The surface tension of gelatin gel in solution and gel states. (b) Nucleation energy required for different bubble sizes and gelatin concentration compared to pure liquid (i.e., water).

rigidity percolation, more triple helical morphology starts to form. In the triple helical configuration, the nonpolar residues are arranged away from the water molecules. The polar molecules preferentially arrange outward of the tropocollagen. Therefore, as time passes during the gelation process the net attractive force between collagen and water molecules increases, thus the surface tension of the gel increases in the gel state [133]. However, gelation process is a chemically dynamic equilibrium state and never ends. The coexistence of the free-floating gelatin monomers (α-chain) and the network is a typical condition in the gel system. Therefore, we have considered both surface tension (solution and gel) as the maximum and minimum limit for the nucleation. In Fig. 22b, we have plotted the nucleation pressure (Eq. (10)) for varying critical nucleation radius and represented as a function of the gel concentration. The vertical bars correspond to the maximum and minimum surface tension. While nucleation pressure for water is 119kPa for $R_o \sim 1.2\ \mu m$, it varies from 142 to 133 kPa for 1% to 10% of gelatin. Considering there exists enough large pore size in the network comparing to the critical bubble size that of water, we will assume this nucleation energy as the base case.

Threshold Tensile Pressure

In this section, we have summarized the extra tensile pressure (ΔP_T) and the critical tensile pressure (P_T). Results from both the strain energy-based criteria (network failure model) and the fracture-based criteria are presented. For the network failure model, the critical condition is set to the fibril failure stretch (λ_f^u) and varied between 35 to 45% strain. Bubble failure stretch (λ_B^u) is used for the fracture-based model and set to $f(\lambda_B^u) = G_c/2R_0$. Two cases are considered for both models, i) critical bubble radius is kept fixed for all gel concentration, and ii) varied based on the unit cell maximum ($R_o = \xi_o/\sqrt{2}$), and pore size maximum ($R_o = L_{MA}/2$). Results are compared with the theoretical range of rubber materials ($\Delta P_T\{max, min\} = \{9G, 5G/2\}$) and experimental data from the drop-tower tests. The vertical bars are used for the results from the network failure model to indicate the maximum and minimum case corresponds to ($S_{gel}\ and\ \lambda_f^u = 1.45$) and ($S_{sol}\ and\ \lambda_f^u = 1.35$), respectively.

Fig. 23 and Fig. 24 show the extra tensile pressure for case (i) and case (ii) described in the previous paragraph, respectively. Both the model predicts extra tensile pressure within the theoretical range for the given gel concentration. For low concentration, ΔP_T does not depend on the critical radius but varies in a wide range for higher gel concentration. $9G$ curve well predicts at the low concentration and overestimates as the concentration increases. $5G/2$ curve does not predict the extra tensile pressure at the low concentration as experimental observation suggests[11]. The network failure model coincides with the theoretical maximum curve for the low concentration. As the concentration increases, the fiber length (ξ_o) and the unit cell volume decrease (see Fig. 7b). It is evident from Fig. 23a that for the same bubble radius, as the concentration increases, the slope of the ΔP_T tends to reduce. The fiber failure strain is reached earlier, and less and less strain energy is required for the bubble to grow unconditionally. The slope reaches an asymptote for higher concentration (C > 5% for $R_o = 1.6\ \mu m$ and C > 10% for $R_o = 0.8\ \mu m$).

Since the gel critical energy release rate linearly increases with the gel concentration for the fracture model, Fig. 23b shows an increasing trend for ΔP_T. In the fracture model, material heterogeneity due to the microstructure is not considered. It is reflected in Fig. 23b as the extra tensile pressure (ΔP_T) significantly depends on G_c and rather slightly over R_o.

Fig. 24 plotted the extra tensile pressure for case (ii), where R_o is a function of gel concentration. Two values of R_o are considered as mentioned earlier. $R_o = L_{MA}/2$ is the lower limit of the maximum possible bubble radius based on the pore size distribution, and extra tensile pressure coincides with the maximum limit given by $9G$ curve. As the maximum limit is based on smaller bubble nuclei with higher surface energy, $R_o = L_{MA}/2$ is more conservative and overestimates the critical tensile pressure. On the other hand, $R_o = \xi_o/\sqrt{2}$ is based on

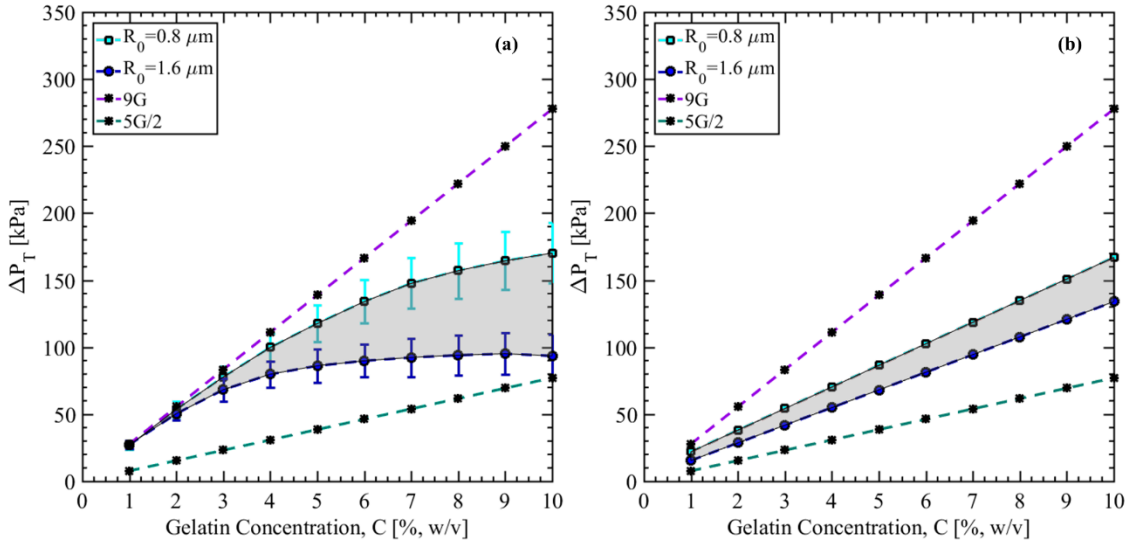

Fig. 23 Extra tensile pressure for fixed critical radius for different gel concentrations. (a) network failure model, and (b) fracture-based model.

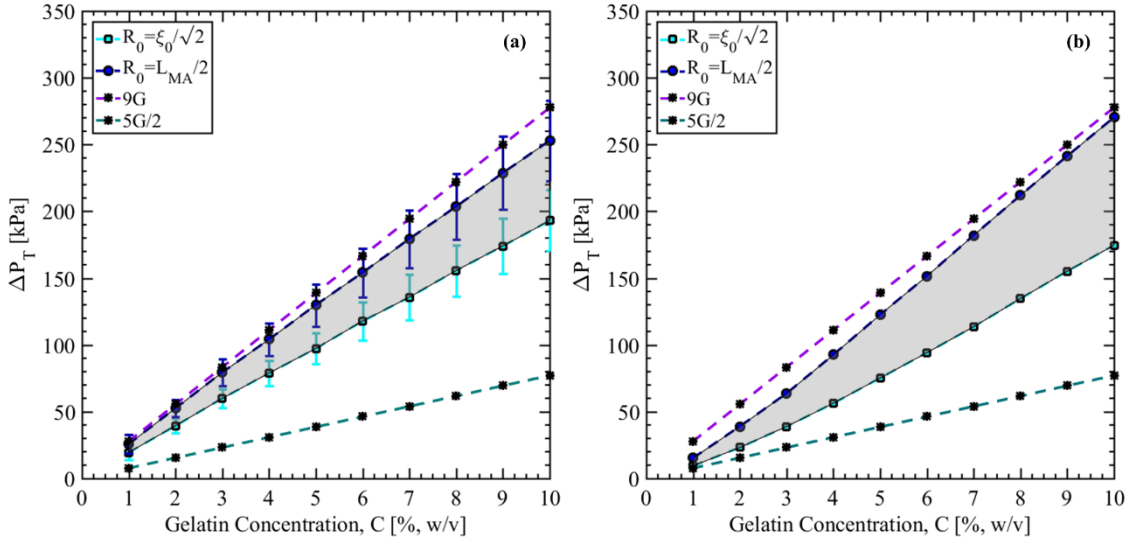

Fig. 24 Extra tensile pressure for varying critical radius (a) network failure model and (b) fracture-based model.

the maximum possible bubble size that can fit in the cubic portion of the unit cell. $R_o = \xi_o/\sqrt{2}$, when used in the network failure model, predicts the most moderate values of the extra tensile pressure. Comparing the network failure model and fracture model in Fig. 24a and 24b, both models predict extra tensile pressure closely (see the shaded regions in Fig. 24). It shows that if R_o is varied based on the microstructure, then our network failure model can predict tensile pressure reasonably well.

Threshold tensile pressure (P_T) is plotted and compared with the experimental data for the case (i) and (ii) in Fig. 25 and Fig. 26, respectively. Results from both network failure and fracture-based models are shown. In Fig. 25a, the best fit is provided by the $R_o = 1.2\mu m$ and can predict the critical tensile pressure for a wide range of gel concentrations for both models. Our intention is not to force-fit the R_o value to predict the tensile pressure and validate the experimental observation. We have considered the range of R_o $(0.8 - 1.6\mu m)$ value based on the nucleation pressure as discussed in the previous section. Although the mean pore size decreases for increasing gel concentrations, large pores are also evident from Fig. 9. It is probable that due to the presence of large pores, even for a highly dense network, the nucleation solely occurs in water. Therefore, we can conclude that in a biphasic (e.g., network and water) hydrogel, nucleation occurs in the liquid phase, and the nucleation pressure for gels is comparable to the nucleation pressure of pure water. Fig. 25b shows the threshold tensile pressure based on the fracture model. In Fig. 26, for case (ii), $R_o = \xi_o/\sqrt{2}$ can predict the critical tensile pressure well for the gel concentration from 3 to 7%. $R_o = L_{MA}/2$ overestimates the critical tensile pressure for both models, as discussed earlier. Both network failure model (Fig. 26a) and fracture model (Fig. 26b) closely predict P_T when R_o is based on the microstructure. Based on all scenarios (Fig. 25 and 26), the fracture model gives

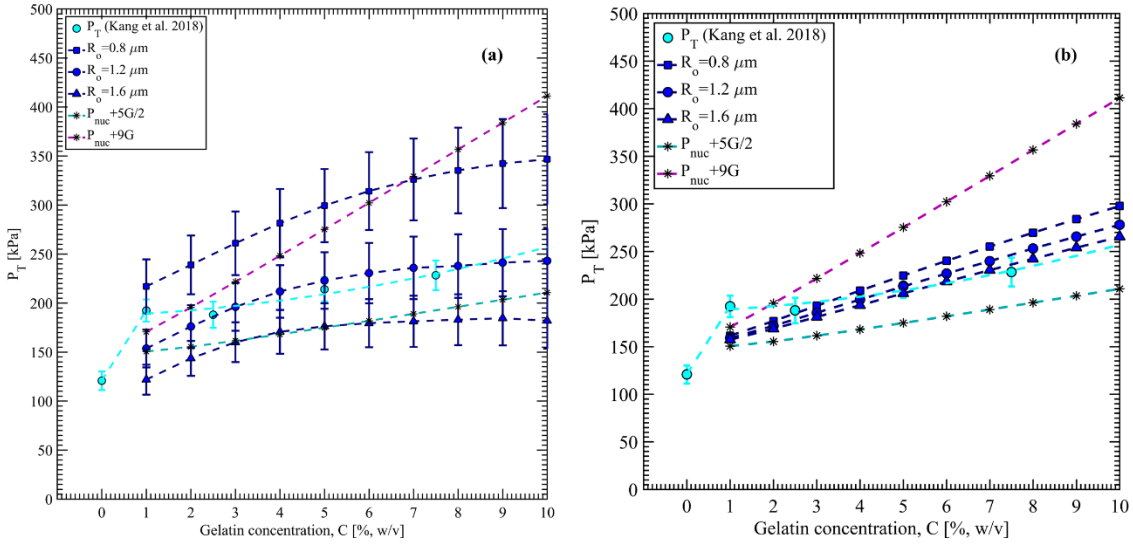

Fig. 25 Threshold tensile pressure for fixed critical bubble radius (case (i)) for different gel concentrations. (a) network failure model and (b) the fracture model.

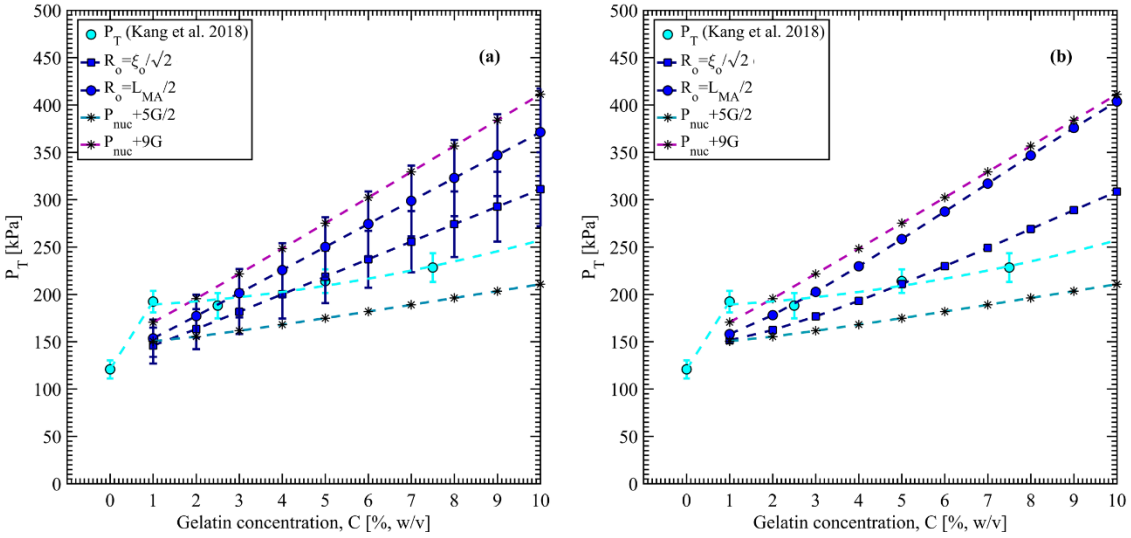

Fig. 26 Threshold tensile pressure for variable critical bubble radius (case (ii)) for different gel concentrations. (a) network failure and (b) the fracture model.

the best prediction when R_o varies within the range of $0.8 - 1.6\mu m$. This also indicates that bubble growth is a fracture phenomenon via material failure, and the effect of microstructure is trivial.

Conclusion

In this manuscript, we have developed a theoretical framework to estimate the critical tensile pressure for cavitation in soft materials. Gelatin gel has been used for modeling purposes since it has various applications in the biomechanics field. Multifunctionality, less toxicity, and less biodegradability are the few reasons gelatin gels are being used for tissue engineering and tissue mechanics. In the first part of this manuscript, we have evaluated the gelatin network topology and then estimated the fiber properties by proposing a unit cell model. A bubble-network interaction is introduced, and strain energy-based failure criteria are then presented based on the microstructure. A fracture-based model is developed as well, and critical tensile pressure is evaluated for both failure criteria. The summary of outcome from this research is as follows,

1. As we have postulated, the nucleation pressure in gelatin is comparable to that of water. A large distribution of the pore size is the basis of this hypothesis. There exist enough large pores that can activate nucleation sites in the range of $\sim 1.2\mu m$.
2. The critical tensile pressure is well predicted by both network failure model and fracture-based model for the critical bubble radius, $R_o \sim 1.2\mu m$.
3. Bubble growth is a fracture-driven event via material failure.
4. The effect of the microstructure is trivial. In the macroscale, more realistic non-linear material properties and critical energy release rate as fracture toughness can reasonably predict the critical threshold tensile pressure.

However, both models underestimate the critical tensile pressure for 1% gel. Since the network rigidity percolation transition happens at the 1% gelatin, an affine network model is not adequate. Just after the network rigidity percolation, there exists a nonaffine domain. Nonaffine network elasticity is bending-dominated and not considered in our proposed model. Nonaffinity is the measure of the heterogeneity of the deformation. Including the degree of the nonaffinity into the network-model, may improve its prediction for the low concentration gels. On the other side of the spectrum, we have a high concentration of gelatin gel (~10%). As the thermal persistence length decreases with increasing concentration, the fibers are more entropic (flexible filament) than enthalpic. Cryo-SEM image observation showed that the fibers could not recoil and form secondary structures at the gelatin's higher crosslinked network. Since the crosslink density increases with increasing concentration, fibers need to be modeled as entropic. Several entropic fiber models are well discussed in the literature, such as the Gaussian, inextensible worm-like-chain (WLC) model, etc. We have not considered this approach since it is beyond the scope of this work.

Author Contributions

Fuad Hasan: Conceptualization, Methodology, Software, Validation, Formal analysis, Investigation, Writing - Original Draft. **KAH Al Mahmud:** Resources, Writing - Review & Editing. **MD Ishak Khan:** Resources, Visualization. **Wonmo Kang:** Conceptualization, Validation. **Ashfaq Adnan:** Conceptualization, Methodology, Validation, Writing - Review & Editing, Funding acquisition.

Conflicts of interest

"There are no conflicts to declare".

Acknowledgements

This work has been funded by the Computational Cellular Biology of Blast (C2B2) program through the Office of Naval Research (ONR) (Award # N00014-18-1-2082- Dr. Timothy Bentley, Program Manager).

Notes and references

1 P. Movahed, W. Kreider, A. D. Maxwell, S. B. Hutchens and J. B. Freund, *J. Acoust. Soc. Am.*, 2016, **140**, 1374–1386.
2 Y. Kurosawa, K. Kato, S. Saito, M. Kubo, T. Uzuka, Y. Fujii and H. Takahashi, in *Proceedings of the 31st Annual International Conference of the IEEE Engineering in Medicine and Biology Society: Engineering the Future of Biomedicine, EMBC 2009*, 2009.
3 F. Hasan, K. A. H. Al Mahmud, M. I. Khan, S. Patil, B. H. Dennis and A. Adnan, *Multiscale Sci. Eng.*, , DOI:10.1007/s42493-021-00060-x.
4 C. C. Church, *J. Acoust. Soc. Am.*, 1989, **86**, 215–227.
5 A. J. Coleman, J. E. Saunders, L. A. Crum and M. Dyson, *Ultrasound Med. Biol.*, 1987, **13**, 69–76.
6 Y. A. Pishchalnikov, O. A. Sapozhnikov, M. R. Bailey, J. C. Williams Jr, R. O. Cleveland, T. Colonius, L. A. Crum, A. P. Evan and J. A. McAteer, *J. Endourol.*, 2003, **17**, 435–446.
7 C. C. Coussios and R. A. Roy, *Annu. Mech.*, 2008, **40**, 395–420.
8 G. A. Husseini, M. A. D. de la Rosa, E. S. Richardson, D. A. Christensen and W. G. Pitt, *J. Control. Release*, 2005, **107**, 253–261.
9 S. Mitragotri, *Nat. Rev. Drug Discov.*, 2005, **4**, 255.
10 W. G. Pitt, G. A. Husseini and B. J. Staples, *Expert Opin. Drug Deliv.*, 2004, **1**, 37–56.
11 J. A. Zimberlin, N. Sanabria-Delong, G. N. Tew and A. J. Crosby, *Soft Matter*, 2007, **3**, 763–767.
12 J. B. Estrada, C. Barajas, D. L. Henann, E. Johnsen and C. Franck, *J. Mech. Phys. Solids*, 2018, **112**, 291–317.
13 S. B. Hutchens, S. Fakhouri and A. J. Crosby, *Soft Matter*, 2016, **12**, 2557–2566.
14 L. Pavlovsky, M. Ganesan, J. G. Younger and M. J. Solomon, *Appl. Phys. Lett.*, 2014, **105**, 3–6.
15 A. Delbos, J. Cui, S. Fakhouri and A. J. Crosby, *Soft Matter*, , DOI:10.1039/c2sm25458a.
16 J. A. Zimberlin and A. J. Crosby, *J. Polym. Sci. Part B Polym. Phys.*, , DOI:10.1002/polb.21968.
17 J. A. Zimberlin, J. J. McManus and A. J. Crosby, *Soft Matter*, , DOI:10.1039/b925407b.
18 J. Cui, C. H. Lee, A. Delbos, J. J. McManus and A. J. Crosby, *Soft Matter*, , DOI:10.1039/c1sm05340j.
19 S. B. Hutchens and A. J. Crosby, *Soft Matter*, , DOI:10.1039/c3sm52689e.
20 W. Yuan-Ting and A. Adnan, *Sci. Reports (Nature Publ. Group)*, 2017, **7**, 1–9.
21 S. Saudi, S. R. Bhattarai, U. Adhikari, S. Khanal, J. Sankar, S. Aravamudhan and N. Bhattarai, *Nanoscale*, 2020, **12**, 23556–23569.
22 J. Goeller, A. Wardlaw, D. Treichler, J. O'Bruba and G. Weiss, *J. Neurotrauma*, 2012, **29**, 1970–1981.
23 A. Nakagawa, G. T. Manley, A. D. Gean, K. Ohtani, R. Armonda, A. Tsukamoto, H. Yamamoto, K. Takayama and T. Tominaga, *J. Neurotrauma*, 2011, **28**, 1101–1119.
24 P. A. Taylor, J. S. Ludwigsen and C. C. Ford, *Brain Inj.*, 2014, **28**, 879–895.
25 L. Zhang, K. H. Yang and A. I. King, *J. Neurotrauma*, 2001, **18**, 21–30.
26 L. Zhang, K. H. Yang and A. I. King, *J. Biomech. Eng.*, 2004, **126**, 226–236.
27 M. I. Khan, F. Hasan, K. A. H. Al Mahmud and A. Adnan, *Multiscale Sci. Eng.*, , DOI:10.1007/s42493-020-00043-4.
28 M. I. Khan, F. Hasan, K. A. Hasan Al Mahmud and A. Adnan, *J. Mech. Behav. Biomed. Mater.*, 2021, **113**, 104149.
29 M. I. Khan, F. Hasan, K. A. H. Al Mahmud and A. Adnan, *Biomolecules*, , DOI:10.3390/biom11040540.
30 M. B. Panzer, B. S. Myers, B. P. Capehart and C. R. Bass, *Ann. Biomed. Eng.*, 2012, **40**, 1530–1544.
31 R. K. Gupta and A. Przekwas, *Front. Neurol.*, 2013, **4 MAY**, 1–21.
32 A. N. Gent and P. B. Lindley, *Rubber Chem. Technol.*, 1958, **31**, 393–394.
33 J. M. Ball, *Philos. Trans. R. Soc. London. Ser. A, Math. Phys. Sci.*, 1982, **306**, 557–611.
34 C. O. Horgan and R. Abeyaratne, *J. Elast.*, 1986, **16**, 189–200.
35 C. O. Horgan and D. A. Polignone, *Appl. Mech. Rev.*, 1995, **48**, 471–485.
36 A. N. Gent and D. A. Tompkins, *J. Appl. Phys.*, 1969, **40**, 2520–2525.
37 C. Fond, *J. Polym. Sci. Part B Polym. Phys.*, 2001, **39**, 2081–2096.
38 A. N. Gent and C. Wang, *J. Mater. Sci.*, 1991, **26**, 3392–3395.
39 A. A. Griffith, *Philos. Trans. R. Soc. london. Ser. A, Contain. Pap. a Math. or Phys. character*, 1921, **221**, 163–198.
40 A. N. Gent, *Rubber Chem. Technol.*, 1990, **63**, 49–53.
41 M. L. Williams and R. A. Schapery, *Int. J. Fract. Mech.*, 1965, **1**, 64–72.
42 Y. Lev and K. Y. Volokh, *J. Appl. Mech. Trans. ASME*, 2016, **83**, 1–4.
43 A. Faye, J. A. Rodríguez-Martínez and K. Y. Volokh, *Int. J. Non. Linear. Mech.*, 2017, **92**, 118–126.
44 O. Lopez-Pamies, M. I. Idiart and T. Nakamura, *J. Mech. Phys. Solids*, 2011, **59**, 1464–1487.
45 O. Lopez-Pamies, T. Nakamura and M. I. Idiart, *J. Mech. Phys. Solids*, 2011, **59**, 1488–1505.
46 A. Kumar, D. Aranda-Iglesias and O. Lopez-Pamies, *J. Elast.*, 2017, **126**, 201–213.
47 V. Lefèvre, K. Ravi-Chandar and O. Lopez-Pamies, *Int. J. Fract.*, 2015, **192**, 0–23.
48 L. R. G. Treloar, *Oxford Univ. Press*.
49 R. H. Pritchard, Y. Y. Shery Huang and E. M. Terentjev, *Soft Matter*, 2014, 10, 1864–1884.
50 G. O. Phillips and P. A. Williams, *Handbook of Hydrocolloids: Second Edition*, 2009.
51 R. Gaudron, M. T. Warnez and E. Johnsen, *J. Fluid Mech.*, 2015, **766**, 54–75.
52 E. P. Stride and C. C. Coussios, *Proc. Inst. Mech. Eng. Part H*

J. Eng. Med., , DOI:10.1243/09544119JEIM622.

53 C. W. Barney, C. E. Dougan, K. R. McLeod, A. Kazemi-Moridani, Y. Zheng, Z. Ye, S. Tiwari, I. Sacligil, R. A. Riggleman, S. Cai, J. H. Lee, S. R. Peyton, G. N. Tew and A. J. Crosby, *Proc. Natl. Acad. Sci. U. S. A.*, 2020.

54 S. Kundu and A. J. Crosby, *Soft Matter*, , DOI:10.1039/b909237d.

55 W. Wang, X. Wu, T. Chantapakul, D. Wang, S. Zhang, X. Ma, T. Ding, X. Ye and D. Liu, *Food Res. Int.*, , DOI:10.1016/j.foodres.2017.09.087.

56 M. J. Madison, G. Coward-Kelly, C. Liang, M. N. Karim, M. Falls and M. T. Holtzapple, *Biomass and Bioenergy*, , DOI:10.1016/j.biombioe.2017.01.007.

57 R. K. Rana, Y. Mastai and A. Gedanken, *Adv. Mater.*, , DOI:10.1002/1521-4095(20021002)14:19<1414::AID-ADMA1414>3.0.CO;2-F.

58 C. E. Brennen, *Cavitation and bubble dynamics*, Cambridge University Press, 2014.

59 W. Kang, A. Adnan, T. O'Shaughnessy and A. Bagchi, *Acta Biomater.*, 2018, **67**, 295–306.

60 K. A. H. Al Mahmud, F. Hasan, M. I. Khan and A. Adnan, *Sci. Rep.*, 2020, **10**, 9635.

61 T. Baumberger, C. Caroli and D. Martina, *Eur. Phys. J. E*, 2006, **21**, 81–89.

62 C. Marmorat, A. Arinstein, N. Koifman, Y. Talmon, E. Zussman and M. Rafailovich, *Sci. Rep.*, 2016, **6**, 6–11.

63 D. Caccavo, S. Cascone, G. Lamberti and A. A. Barba, *Chem. Soc. Rev.*, 2018, 47, 2357–2373.

64 Q. Chai, Y. Jiao and X. Yu, *Gels*, 2017, **3**, 6.

65 A. Karoyo and L. Wilson, *Gels*, 2017, **3**, 1.

66 A. Duconseille, T. Astruc, N. Quintana, F. Meersman and V. Sante-Lhoutellier, *Food Hydrocoll.*, 2015, 43, 360–376.

67 S. Paul, M. Motalab, M. A. Zobayer and M. J. Hossain, *J. Adhes. Sci. Technol.*, 2017, **31**, 1782–1795.

68 S. Z. Bonyadi, M. M. Hasan, J. Kim, S. Mahmood, K. D. Schulze and A. C. Dunn, *Tribol. Lett.*, 2020, **68**, 119.

69 K. Paul and L. Ladani, *SN Appl. Sci.*, 2020, **2**, 1418.

70 R. C. Picu, *Soft Matter*, 2011, 7, 6768–6785.

71 C. P. Broedersz and F. C. Mackintosh, *Rev. Mod. Phys.*, 2014, **86**, 995–1036.

72 K. Linka, M. Hillgärtner and M. Itskov, *Acta Biomater.*, 2018, **71**, 398–410.

73 M. Hillgärtner, K. Linka and M. Itskov, *J. Biomech.*, 2018, **80**, 129–135.

74 A. Kabla and L. Mahadevan, *J. R. Soc. Interface*, 2007, **4**, 99–106.

75 E. Kuhl, K. Garikipati, E. M. Arruda and K. Grosh, *J. Mech. Phys. Solids*, 2005, **53**, 1552–1573.

76 J. E. Bischoff, E. A. Arruda and K. Grosh, *J. Appl. Mech. Trans. ASME*, 2002, **69**, 570–579.

77 M. E. Susilo, B. A. Roeder, S. L. Voytik-Harbin, K. Kokini and E. A. Nauman, *Acta Biomater.*, 2010, **6**, 1471–1486.

78 G. A. Holzapfel and R. W. Ogden Editors, *Biomechanics: Trends in Modeling and Simulation*, 2014.

79 S. P. Lake, M. F. Hadi, V. K. Lai and V. H. Barocas, *Ann. Biomed. Eng.*, 2012, **40**, 2111–2121.

80 R. C. Picu, S. Deogekar and M. R. Islam, *J. Biomech. Eng.*, 2018, **140**, 1–12.

81 L. Zhang, S. P. Lake, V. K. Lai, C. R. Picu, V. H. Barocas and M. S. Shephard, *J. Biomech. Eng.*, 2013, **135**, 1–9.

82 A. M. Stein, D. A. Vader, D. A. Weitz and L. M. Sander, *Complexity*, 2011, **16**, 22–28.

83 A. M. STEIN, D. A. VADER, L. M. JAWERTH, D. A. WEITZ and L. M. SANDER, *J. Microsc.*, 2008, **232**, 463–475.

84 B. Lee, X. Zhou, K. Riching, K. W. Eliceiri, P. J. Keely, S. A. Guelcher, A. M. Weaver and Y. Jiang, *PLoS One*, 2014, **9**, 1–12.

85 P. L. Chandran, T. Stylianopoulos and V. H. Barocas, *Multiscale Model. Simul.*, 2008, **7**, 22–43.

86 P. L. Chandran and V. H. Barocas, *J. Biomech. Eng.*, 2006, **128**, 259–270.

87 D. A. Head, A. J. Levine and F. C. MacKintosh, *Phys. Rev. E*, 2003, **68**, 61907.

88 S. B. Lindström, A. Kulachenko, L. M. Jawerth and D. A. Vader, *Soft Matter*, 2013, **9**, 7302–7313.

89 H. Bechir, L. Chevalier and M. Idjeri, *Int. J. Eng. Sci.*, , DOI:10.1016/j.ijengsci.2009.10.004.

90 M. C. Wang and E. Guth, *J. Chem. Phys.*, 1952, **20**, 1144–1157.

91 P. J. Flory and J. Rehner Jr, *J. Chem. Phys.*, 1943, **11**, 512–520.

92 L. R. G. Treloar, *Trans. Faraday Soc.*, 1946, **42**, 77–82.

93 E. M. Arruda and M. C. Boyce, *J. Mech. Phys. Solids*, 1993, **41**, 389–412.

94 M. C. Boyce, *Rubber Chem. Technol.*, 1996, **69**, 781–785.

95 P. K. Purohit, R. I. Litvinov, A. E. X. Brown, D. E. Discher and J. W. Weisel, *Acta Biomater.*, 2011, **7**, 2374–2383.

96 K. Bertoldi and M. C. Boyce, *J. Mater. Sci.*, 2007, **42**, 8943–8956.

97 R. Stringfellow and R. Abeyaratne, *Mater. Sci. Eng. A*, , DOI:10.1016/0921-5093(89)90351-1.

98 A. N. Gent, P. B. Lindley and E. K. Rideal, *Proc. R. Soc. London. Ser. A. Math. Phys. Sci.*, 1959, **249**, 195–205.

99 G. H. Lindsey, *J. Appl. Phys.*, , DOI:10.1063/1.1709232.

100 Y. Y. Lin and C. Y. Hui, *Int. J. Fract.*, , DOI:10.1023/B:FRAC.0000026510.60747.3a.

101 S. Raayai-Ardakani, D. R. Earl and T. Cohen, *Soft Matter*, 2019, **15**, 4999–5005.

102 R. W. Ogden and P. R. S. L. A, *Proc. R. Soc. London. A. Math. Phys. Sci.*, 1972, **326**, 565–584.

103 C. C. Church, *Ultrasound Med. Biol.*, 2002, **28**, 1349–1364.

104 J. Herbertz, *Fortschritte der Akust. DAGA*, 1988, **14**, 439.

105 V. P. Carey, *Liquid-vapor phase-change phenomena: an introduction to the thermophysics of vaporization and condensation processes in heat transfer equipment*, CRC Press, 2020.

106 M. Fang and M. M. B. Holl, *Bonekey Rep.*, , DOI:10.1038/bonekey.2013.128.

107 P. B. Welzel, S. Prokoph, A. Zieris, M. Grimmer, S. Zschoche, U. Freudenberg and C. Werner, *Polymers (Basel).*, , DOI:10.3390/polym3010602.

108 F. C. Mackintosh, J. Kas and P. A. Janmey, *Phys. Rev. Lett.*, 1995, **75**, 4425.

109 L. R. G. Treloar, *Polymer (Guildf).*, , DOI:10.1016/0032-

3861(60)90012-4.
110 A. Markidou, W. Y. Shih and W.-H. Shih, *Rev. Sci. Instrum.*, 2005, **76**, 64302.
111 S. Ma, M. Natoli, X. Liu, M. P. Neubauer, F. M. Watt, A. Fery and W. T. S. Huck, *J. Mater. Chem. B*, , DOI:10.1039/c3tb20851f.
112 B. Mohanty and H. B. Bohidar, *Int. J. Biol. Macromol.*, 2005, **36**, 39–46.
113 N. A. Hotaling, K. Bharti, H. Kriel and C. G. Simon Jr, *Biomaterials*, 2015, **61**, 327–338.
114 J. Schindelin and others, .
115 J. P. R. O. Orgel, T. C. Irving, A. Miller and T. J. Wess, *Proc. Natl. Acad. Sci. U. S. A.*, 2006, **103**, 9001–9005.
116 M. F. Hadi and V. H. Barocas, *J. Biomech. Eng.*, 2013, **135**, 1–8.
117 M. Czerner, L. A. Fasce, J. F. Martucci, R. Ruseckaite and P. M. Frontini, *Food Hydrocoll.*, 2016, **60**, 299–307.
118 B. A. Roeder, K. Kokini, J. E. Sturgis, J. P. Robinson and S. L. Voytik-Harbin, *J. Biomech. Eng.*, 2002, **124**, 214–222.
119 Y. Tang, R. Ballarini, M. J. Buehler and S. J. Eppell, *J. R. Soc. Interface*, 2010, **7**, 839–850.
120 Y. C. Fung and R. Skalak, *J. Biomech. Eng.*, , DOI:10.1115/1.3138285.
121 F. H. Silver and D. L. Christiansen, *Biomaterials Science and Biocompatibility*, 1999.
122 P. BORNSTEIN and W. TRAUB, in *The Proteins*, 1979.
123 J. S. Graham, A. N. Vomund, C. L. Phillips and M. Grandbois, *Exp. Cell Res.*, 2004, **299**, 335–342.
124 J. A. J. J. Van Der Rijt, K. O. Van Der Werf, M. L. Bennink, P. J. Dijkstra and J. Feijen, *Macromol. Biosci.*, 2006, **6**, 697–702.
125 M. P. E. Wenger, L. Bozec, M. A. Horton and P. Mesquidaz, *Biophys. J.*, 2007, **93**, 1255–1263.
126 A. A. Griffith and J. J. Gilman, *Trans. ASM*, 1968, **61**, 855–906.
127 A. E. Forte, F. D'amico, M. N. Charalambides, D. Dini and J. G. Williams, *Food Hydrocoll.*, 2015, **46**, 180–190.
128 X. Yang and C. C. Church, *J. Acoust. Soc. Am.*, 2005, **118**, 3595–3606.
129 S. H. Min and M. L. Berkowitz, *J. Chem. Phys.*, , DOI:10.1063/1.5079735.
130 Y. (陈燕) Chen, A. Islam, M. Sussman and Y. Lian, *Phys. Fluids*, 2020, **32**, 122117.
131 J. H. Johnston, *Biochem. J.*, , DOI:10.1042/bj0211314.
132 H. Sato and K. Ueberreiter, *Die Makromol. Chemie Macromol. Chem. Phys.*, 1979, **180**, 829–835.
133 M. P. McGee, M. Morykwas, J. Shelton and L. Argenta, *Biophys. J.*, , DOI:10.1016/j.bpj.2012.10.010.